

# NAVAL POSTGRADUATE SCHOOL MONTEREY, CALIFORNIA



## THESIS

### LIMIT-CYCLE BEHAVIOR IN FREE ELECTRON LASERS

by

Roger M. Mabe

December, 1995

Thesis Advisors:

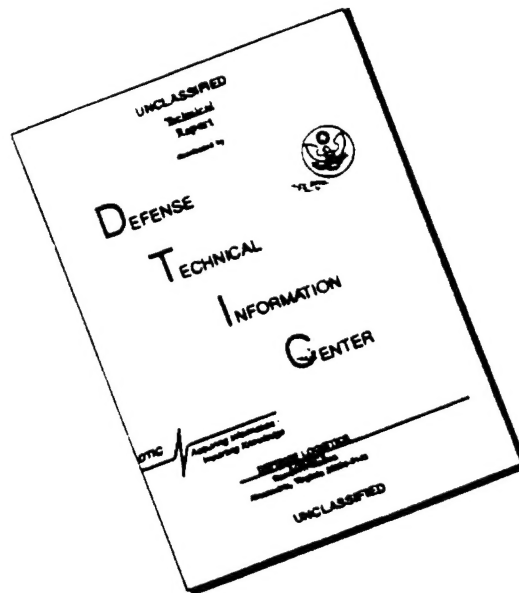
Robert L. Armstead  
William B. Colson

Approved for public release; distribution is unlimited.

19960326 045

DTIC QUALITY INSPECTED 1

# DISCLAIMER NOTICE



THIS DOCUMENT IS BEST QUALITY AVAILABLE. THE COPY FURNISHED TO DTIC CONTAINED A SIGNIFICANT NUMBER OF PAGES WHICH DO NOT REPRODUCE LEGIBLY.

REPORT DOCUMENTATION PAGE			Form Approved OMB No. 0704-0188	
Public reporting burden for this collection of information is estimated to average 1 hour per response, including the time for reviewing instruction, searching existing data sources, gathering and maintaining the data needed, and completing and reviewing the collection of information. Send comments regarding this burden estimate or any other aspect of this collection of information, including suggestions for reducing this burden, to Washington Headquarters Services, Directorate for Information Operations and Reports, 1215 Jefferson Davis Highway, Suite 1204, Arlington, VA 22202-4302, and to the Office of Management and Budget, Paperwork Reduction Project (0704-0188) Washington DC 20503.				
1. AGENCY USE ONLY (Leave blank)		2. REPORT DATE December, 1995		3. REPORT TYPE AND DATES COVERED Master's Thesis
4. TITLE AND SUBTITLE LIMIT-CYCLE BEHAVIOR IN FREE ELECTRON LASERS (u)			5. FUNDING NUMBERS	
6. AUTHOR(S) Roger M. Mabe				
7. PERFORMING ORGANIZATION NAME(S) AND ADDRESS(ES) Naval Postgraduate School Monterey CA 93943-5000			8. PERFORMING ORGANIZATION REPORT NUMBER	
9. SPONSORING/MONITORING AGENCY NAME(S) AND ADDRESS(ES)			10. SPONSORING/MONITORING AGENCY REPORT NUMBER	
11. SUPPLEMENTARY NOTES The views expressed in this thesis are those of the author and do not reflect the official policy or position of the Department of Defense or the U.S. Government.				
12a. DISTRIBUTION/AVAILABILITY STATEMENT Approved for public release; distribution is unlimited.			12b. DISTRIBUTION CODE	
13. ABSTRACT (maximum 200 words) Many Free Electron Lasers (FEL) are driven by short electron pulses which create equally short optical pulses. At saturation, the strong optical fields present in the undulator result in the trapped-particle instability which drives the carrier wave unstable and modulates the optical pulse. The trapped-particle instability coupled with the short optical pulses can result in periodic oscillations of the pulse shape. This results in oscillations of the output power even though all input parameters are constant. The effect is known as limit-cycle behavior. The character of the oscillation is highly nonlinear and is dependent on the physical input parameters of the current density, resonator losses, electron pulse length, and desynchronism of the resonator cavity. These power oscillations affect the operation of the FEL requiring better insight into their cause and control. Using simulations based on a self consistent Maxwell-Lorentz theory of FEL operation, the dependence of the limit-cycle oscillations on these physical parameters is examined.				
14. SUBJECT TERMS Free Electron Laser, Limit-Cycle Behavior, Power Oscillations			15. NUMBER OF PAGES 85	
			16. PRICE CODE	
17. SECURITY CLASSIFICATION OF REPORT Unclassified	18. SECURITY CLASSIFICATION OF THIS PAGE Unclassified	19. SECURITY CLASSIFICATION OF ABSTRACT Unclassified	20. LIMITATION OF ABSTRACT UL	

NSN 7540-01-280-5500

Standard Form 298 (Rev. 2-89)  
Prescribed by ANSI Std. Z39-18 298-102





Approved for public release: distribution is unlimited.

## LIMIT-CYCLE BEHAVIOR IN FREE ELECTRON LASERS

**R. M. Mabe**

Lieutenant Commander, United States Navy

B. S., North Carolina State University, 1982

Submitted in partial fulfillment of the  
requirements for the degree of

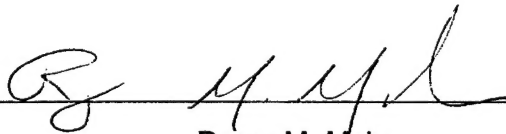
**MASTER OF SCIENCE IN PHYSICS**

from the

**NAVAL POSTGRADUATE SCHOOL**

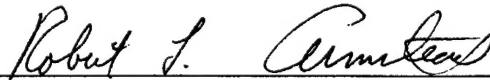
December 1995

Author:

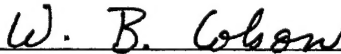


Roger M. Mabe

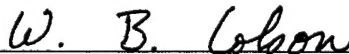
Approved by:



Robert L. Armstead, Thesis Advisor



William B. Colson, Thesis Advisor



William B. Colson, Chairman,

Department of Physics



## **ABSTRACT**

Many Free Electron Lasers (FEL) are driven by short electron pulses which create equally short optical pulses. At saturation, the strong optical fields present in the undulator result in the trapped-particle instability which drives the carrier wave unstable and modulates the optical pulse. The trapped-particle instability coupled with the short optical pulses can result in periodic oscillations of the pulse shape. This results in oscillations of the output power even though all input parameters are constant. The effect is known as limit-cycle behavior.

The character of the oscillation is highly nonlinear and is dependent on the physical input parameters of the current density, resonator losses, electron pulse length and desynchronism of the resonator cavity. These power oscillations affect the operation of the FEL, requiring better insight into their cause and control. Using simulations based on a self consistent Maxwell-Lorentz theory of FEL operation, the dependence of the limit-cycle oscillations on these physical parameters is examined.



# TABLE OF CONTENTS

I. INTRODUCTION .....	1
A. HISTORY .....	1
B. THE CASE FOR A SHIP BASED FEL .....	2
1. Inadequacy of Kinetic Kill Weapons .....	2
2. Lasers Against Missiles .....	3
3. Why the FEL is a Good Choice .....	5
C. FEL COMPONENTS .....	5
II. FEL THEORY .....	9
A. BASIC OPERATION .....	9
B. ELECTRON DYNAMICS INSIDE A HELICAL UNDULATOR .....	11
C. THE OPTICAL WAVE EQUATION .....	16
D. LOW-CURRENT LOW GAIN FEL .....	19
E. STRONG OPTICAL FIELDS .....	23
F. MODE COMPETITION AND COHERENCE DEVELOPMENT .....	26
G. LONGITUDINAL MULTIMODE THEORY .....	28
H. TRAPPED PARTICLE INSTABILITY .....	29
III. LIMIT-CYCLE BEHAVIOR .....	35
A. SHORT PULSE THEORY .....	35
B. LIMIT-CYCLE BEHAVIOR .....	39
C. EFFECTS OF PHYSICAL CONTROL PARAMETERS .....	44
1. Current Density .....	45
2. Resonator Quality Factor .....	50
3. Electron Pulse Width .....	56

4. Desynchronism .....	61
IV. CONCLUSIONS .....	69
LIST OF REFERENCES .....	71
INITIAL DISTRIBUTION LIST .....	73

## **ACKNOWLEDGEMENT**

The author is grateful for support of this work by the Naval Postgraduate School. The author would also like to thank W. B. Colson and R. L. Armstead for their invaluable assistance. The author owes a special debt of gratitude to Suzan, Isaac, and Jacob for the time that should have been theirs.





# I. INTRODUCTION

## A. HISTORY

The Free Electron Laser (FEL) uses a beam of relativistic electrons traveling through a transverse magnetic field to generate coherent radiation. The concept of the Free Electron Laser (FEL) is a natural extension of microwave tube generation of coherent radiation using free electrons. These generally used structures that modified the electromagnetic wave to couple the electrons for energy exchange. However, these structures only work well for wavelengths greater than 1 mm. Another method is needed to couple the electrons to the electromagnetic wave in order to generate coherent radiation in the shorter wavelengths.

In 1951, Hans Motz amplified an electromagnetic beam by propagating it collinear with a beam of electrons traveling through a transverse magnetic field produced by an undulator magnet [1]. In 1960, Robert Phillips developed a device called the ubitron, similar in operation to an FEL [1]. In 1970, John Madey at Stanford University proposed the FEL in its current form and used quantum mechanical theory to explain its operation [1]. Using his theory, he showed the operation of the FEL was based on stimulated emission of radiation. In 1976, Madey succeeded in demonstrating gain with an FEL, amplifying the output from a CO<sub>2</sub> laser operating at 10  $\mu\text{m}$  [1]. The possibility of a tunable high power laser arose in 1977 when D. A. G. Deacon et. al. using the Stanford FEL, lased the device at 3.5  $\mu\text{m}$  [1].

The possibility of a high power tunable laser also generated interest in the military aspects of such a weapon and in 1978 the Defense Advanced Research Projects Agency (DARPA) began studies into the feasibility of the FEL as a weapon system. These studies resulted in experiments conducted by TRW, Math Sciences Northwest, and Los Alamos National Laboratory (LANL) for the construction of a multi-megawatt FEL. The success of the LANL experiment continued into the early 1980's [2]. By the mid 1980's the Strategic Defense Initiative Organization (SDIO) had been established

and the FEL programs at the national laboratories came under its auspices. The laboratories and industry, Boeing Aircraft Corporation and LANL, and TRW and Lawrence Livermore National Laboratory (LLNL) began competition on a multi-megawatt range Ground Based FEL (GBFEL). The Boeing/LANL team won production of the GBFEL. However, in the early 1990's SDIO shifted its emphasis from directed energy to kinetic kill weapons. Funding for the GBFEL was cut annually until the program was finally terminated in 1993. The SDIO was unable to produce a high power FEL weapon and today there is no funded FEL weapon program.

During the same period, other non-military uses of the FEL came to fruition. The real time adaptability of the FEL makes it an ideal tool for use in laser surgery [3]. Other potential uses include industrial processing for applications as diverse as fabrication of semiconductor circuits to synthetic fiber treatment. The FEL may also be used in fusion inertial confinement systems [3]. The flexibility of the FEL continue to make it an attractive alternative to conventional lasers for both military and non-military purposes. Today, there are approximately 20 FELs in operation and another 40 or more in various stages of production.

## **B. THE CASE FOR A SHIP BASED FREE ELECTRON LASER SYSTEM**

### **1. The Inadequacy of Kinetic Kill Weapons**

Transonic and supersonic missiles pose a great threat to modern warships. Present means of defense consist of blasting the incoming missile with high speed ( $\approx 1000$  m/s) dense projectiles. Although these systems can detect the missile at ranges of 10 km or more, firing limitations prevent engagement until the missile closes to ranges of approximately 2000 m. A missile traveling at Mach 1 closes the ship approximately 1000 m every three seconds. Nominally, about six projectiles are required to destroy the missile. The angular distribution of projectiles around the aim point of present kinetic kill weapon systems is such that the missile usually closes to less than 500 m of the ship before these systems can achieve a high probability of kill.

Within this range debris from the destroyed missile may still reach the ship and cause significant damage. A system which can engage and destroy the missile at greater ranges is needed.

## 2. Lasers against Missiles

A laser-based system can focus large amounts of energy at the missile and is a better alternative. The laser beam can reach the missile nearly instantaneously. To be destroyed an incoming missile must absorb an energy density generally referred to as fluence. A moderately hardened missile will have a fluence of approximately 10 kJ/cm<sup>2</sup> [4]. This amount of fluence requires an irradiance of 10 kW/cm<sup>2</sup> focused for a second at the target. However, the total transmitted power cannot simply be the diffraction-corrected power density. Propagation of a high power laser beam through the atmosphere is subject to a variety of effects which affect the amount of power delivered on target [5].

As the laser beam propagates to the target through the atmosphere, it is subjected to linear absorption and scattering due to the molecular and aerosol constituents. It is also subjected to random wander, spreading, and distortion of the beam due to atmospheric turbulence and thermal blooming resulting from the absorption of small amounts of the beam power. Finally, at high intensities it is attenuated due to plasmas resulting from gas breakdown of the atmosphere. [5]. These effects are dependent on the condition of the atmosphere, wavelength, and the operational mode of the laser. The effects of absorption, scattering, and turbulence are approximated by:

$$I_p = \frac{P}{\pi a^2} e^{-\alpha_t z}, \quad (1.1)$$

where  $I_p$  is the peak irradiance at a range  $z$ ,  $P$  is the total transmitted power,  $a$  is the  $1/e$  radius of the Gaussian beam and accounts for the effects of diffraction, source beam quality, jitter, and atmospheric turbulence, and  $\alpha_t$  is the total attenuation

coefficient for scattering and absorption [5]. The extinction coefficient,  $\alpha_t$ , is a complicated function of wavelength. Figure 1 shows total extinction for wavelengths between 0.5  $\mu\text{m}$  and 15  $\mu\text{m}$  in a maritime environment [6]. Within this wavelength interval exists wavelengths which experience 100% extinction along with regions which experience relatively little extinction.

## Maritime HEL Propagation

### Total Extinction

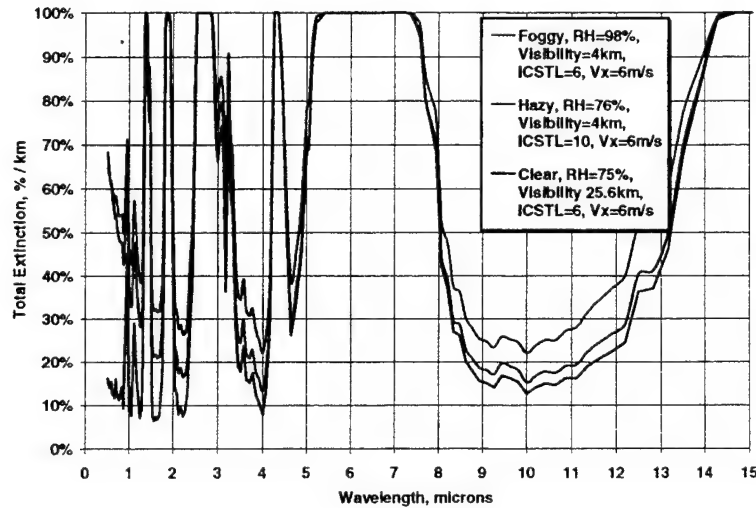


Figure 1. Spectral Extinction in a Maritime Environment from 0.5  $\mu\text{m}$  to 15  $\mu\text{m}$ . (Spectrum is from LOTRAN simulations with standard maritime aerosol model conducted by the High Energy Laser Systems Test Facility (HELSTF) weather station [6])

At first glance, increasing the power transmitted might seem a solution to the problem of extinction. However, increasing the power increases the power absorbed by the atmosphere and worsens the thermal blooming effect. Thermal blooming refers to the self-induced distortion of the beam resulting from heating of the atmosphere as

the beam propagates through it. The heating causes density changes which result in local index of refraction gradients. These index of refraction gradients act as a distributed lens which distort the beam and can limit the maximum irradiance that can be delivered to the target [5]. The effect is strongest at locations along the beam path where the effects of cross-winds and beam slew-rate are equal creating areas where the relative wind velocity is zero, also known as stagnation points.

### **3. Why the FEL is a Good Choice**

The attenuation of the beam by the atmosphere is wavelength dependent. At certain wavelengths "windows" exist which result in a higher irradiance at the target for a given initial beam power. The lower power of the beam also minimizes the thermal blooming effect. The combined effect is to limit the maximum amount of power that can be propagated to the target at a given wavelength. This can be seen in Figure 2, which shows the average irradiance at 5 km for various wavelengths for a given transmission power [6]. A high power laser system which can be tuned to the proper wavelength and maintain a narrow bandwidth is necessary. The ability to construct the FEL for operation in a given wavelength range makes it the logical choice.

### **C. FEL COMPONENTS**

A typical FEL consists of an relativistic electron beam produced by an accelerator, electron beam focusing elements, undulator of length  $L$ , optical resonator (oscillator only), and possibly an electron beam energy recovery system. The basic arrangement is shown in Figure 3.

The purpose of the undulator is to periodically deflect the electrons transversely as they travel along the optical mode axis. This motion allows energy transfer between the electron and optical beams. The resonator stores the optical power, out couples the optical beam for use, and enhances coupling of the optical mode to the electron beam. A coherent, freely propagating optical wave of a given cross-sectional

# Search for Wavelength Options

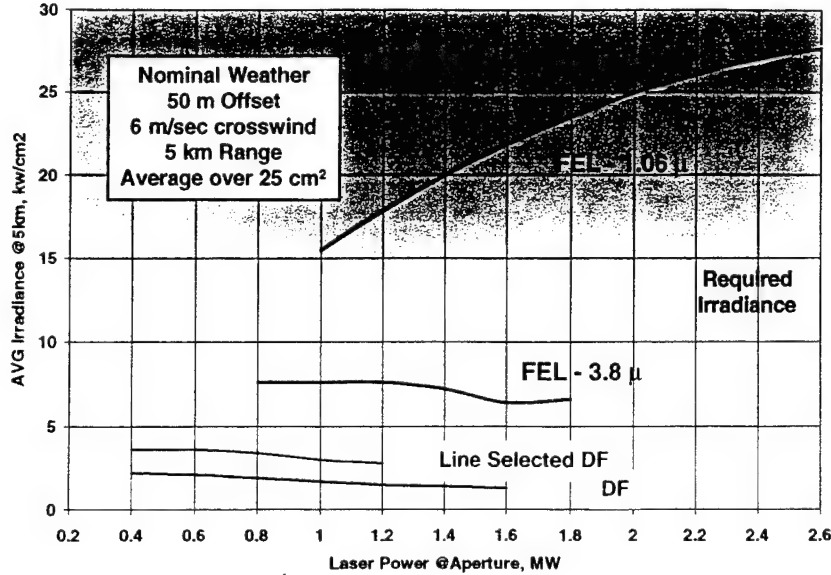


Figure 2. Average irradiance at 5 km for various wavelengths for a given Laser Transmission Power. ( Average irradiance based on simulations conducted by MIT/Lincoln Labs[6])

area will double its cross-sectional area over a distance known as the Rayleigh length,  $\pi w_o^2/\lambda$ , where  $w_o$  is the initial beam waist size and  $\lambda$  is the optical wavelength. If the optical mode waist becomes larger than the electron beam radius,  $r_b$  over the interaction region,  $L$ , the FEL coupling is reduced. The Rayleigh length is made comparable to the undulator length to ensure adequate coupling [1].

The undulator consists of a spatially alternating magnetic field of  $N$  periods with a wavelength  $\lambda_o = L/N$ . A typical undulator wavelength is 2 cm to 10 cm extending over 20 to several hundred periods, making the undulator 1 m to 20 m in length. The peak magnetic field strength is typically 2 kG to 7 kG. During operation only the electron beam and optical wave are present in the undulator, hence there is no internal structure to be destroyed during high power operation.

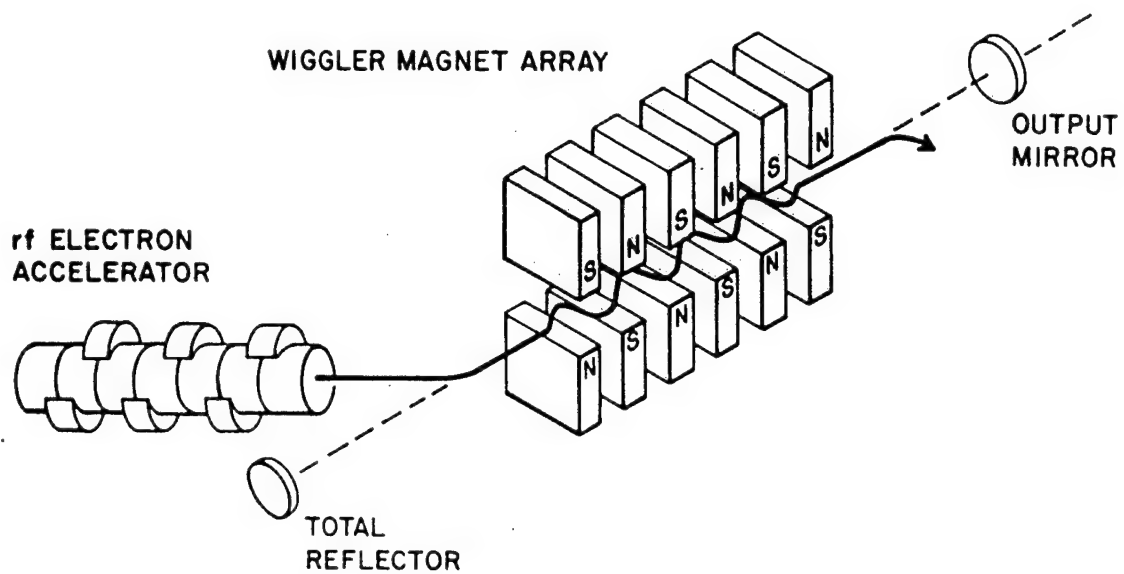


Figure 3. Basic FEL arrangement showing the accelerator, undulator (wiggler), and resonator. From [3].





## II. FEL THEORY

### A. BASIC OPERATION

The operation of the FEL depends on the interaction between the electron beam, the electric and magnetic fields of the optical beam, and the magnetic field of the undulator. In the FEL, gain develops from coherent electron bunching on the scale of the radiation wavelength. The electrons travel at relativistic speeds and are accelerated from side to side as they pass through the undulator field. Radiation from electrons traveling at relativistic velocities is confined to a narrow cone about the forward direction of their motion [1]. In the FEL oscillator, this radiation is stored in an optical resonator. In the FEL amplifier, this radiation adds coherently to an incident optical beam. In either arrangement, the optical beam propagates colinear with the electron beam through the undulator. The electrons are accelerated in the presence of the radiation field. As the relativistic electrons travel through the undulator, in the electron frame of reference the undulator periods are Lorentz contracted to a shorter wavelength,  $\lambda_o' = \lambda_o/\gamma$ , where  $\gamma$  is the electrons' Lorentz factor. The electrons also interact with a radiation field Doppler shifted to a longer wavelength by  $\lambda' = (1 + \beta_z)\gamma\lambda \approx 2\gamma\lambda$ . At resonance  $\lambda' = \lambda_o'$  and gives the FEL resonance condition in the laboratory frame,  $\lambda \approx \lambda_o/2\gamma^2$  [1]. This condition is one of the most important features of the FEL: its continuous tunability. As the electron beam energy is changed the resonant optical wavelength of the FEL also changes.

In order for an electron to transfer energy to the radiation field, its velocity vector must be parallel to the optical wave electric field vector:

$$\dot{\gamma} = \frac{e}{mc} \vec{\beta} \cdot \vec{E}_s, \quad (2.1)$$

where  $\dot{\gamma}$  is the time rate of change of the Lorentz factor of the electron and is proportional to the rate of change of the electron's energy,  $\vec{\beta}$  is the the ratio of the

electron's velocity vector to the speed of light,  $c$ ,  $\vec{E}_s$  is the electric field vector of the radiation, and  $m$  is the mass of the electron. When an electron travels colinearly with an electromagnetic wave there is no energy transfer since the electron's velocity vector and the electric field vector are perpendicular. For energy transfer, components of the electron's velocity must be made parallel to the optical wave electric field vector. This arrangement can be established in a number of ways. For example, the interaction can be established by propagating a TM electromagnetic wave in a rectangular waveguide. The TM wave will have an axial electric field component which can interact with electrons traveling along the axial direction in the waveguide. This is the basis of operation of the traveling-wave tube. However, this arrangement is only feasible for wavelengths longer than about 1 mm, since the axial field amplitude decays away from the walls of the structure in a distance of about  $\lambda\gamma/4\pi$  [1]. In the FEL, the electron's trajectory is deflected in the transverse direction by the interaction with the undulator magnetic field. Thus, the electron is given a transverse velocity component that is parallel to the electric field of the colinearly propagating electromagnetic wave. This deflection of the electron trajectories establishes an important part of the FEL interaction.

The rest of the interaction occurs on the scale of the optical wavelength. As the electrons are accelerated in the transverse direction in the undulator, they radiate. The electrons are initially at random positions in the electron beam, and the electromagnetic radiation an electron emits is at a random phase with respect to that emitted by the other electrons in the beam. The field amplitude resulting from these random phased electromagnetic waves is proportional to  $\sqrt{n_e}$ , where  $n_e$  is the number of electrons in the beam [3]. The power will be proportional to the square of the field amplitude and thus to  $n_e$ . When the electrons travel through the undulator in the presence of an electromagnetic wave, they also interact with the electromagnetic fields of the optical wave. At resonance, the transverse accelerations due to the undulator are the same frequency as the oscillations of the electric field vector of the optical

wave [1]. The electron beam pulse is usually on the order of many optical wavelengths in length with many electrons ( $\approx 10^6$ ) in each optical wavelength so that the electrons can be considered distributed uniformly along the electromagnetic wave. As the electrons travel through the undulator, some electrons will be given velocity components that are parallel to the wave's electric field vector and lose energy; some electrons will be given velocity components that are anti-parallel to the electric field vector and gain energy. Therefore, some electrons speed up and some slow down. The faster electrons catch the slower moving electrons and "bunch". The once uniformly distributed electron beam becomes bunched on the order of the optical wavelength. This bunching is also part of the FEL interaction.

The electrons, now bunched in position, radiate relatively in phase with each other and with the copropagating optical wave. The amplitude of the now coherent radiation is proportional to  $n_e$  and the power is proportional to  $n_e^2$  [3]. Since the number of electrons is typically large, the coherent power is much greater than the incoherent power. Since  $n_e$  is proportional to the current of the electron beam, the coherent power is proportional to the square of the current. The amplification of the incident optical wave amplitude is proportional to the input electron beam current.

## B. ELECTRON DYNAMICS INSIDE A HELICAL UNDULATOR

In order to understand the dynamics of the FEL interaction, the interaction between the electrons, the optical wave fields, and the undulator magnetic field must be examined. The derivation assumes the FEL has a helical undulator in operation with an initial optical field amplitude  $E$ . A helical undulator is assumed since the motion of electrons is simpler. The evolution of the optical wave will be governed by Maxwell's equations. The evolution of the electrons will be governed by the Lorentz force equation. An ideal helical undulator magnetic field will be given by:

$$\vec{B} = B( \cos(k_o z), \sin(k_o z), 0 ) , \quad (2.2)$$

where  $k_o = 2\pi/\lambda_o$  is the undulator wavenumber, and  $B$  is the magnetic field amplitude. Electrons traveling through a helical undulator will produce a circularly polarized plane electromagnetic wave described by:

$$\vec{E}_s = E(\cos\psi, -\sin\psi, 0), \vec{B}_s = E(\sin\psi, \cos\psi, 0), \quad (2.3)$$

where  $\psi = kz - \omega t + \phi$  is the phase of the optical wave with wavenumber  $k = 2\pi/\lambda$ , angular frequency  $\omega = kc = 2\pi f$ , and optical phase  $\phi$ . The forces on an electron are given by the Lorentz force equation [7]:

$$\frac{d\vec{p}}{dt} = -e[\vec{E} + \frac{\vec{v}}{c} \times \vec{B}], \quad (2.4)$$

where  $\vec{p} = \gamma m \vec{v}$  is the electron momentum. The change in the electron energy resulting from the Lorentz force is given by:

$$\frac{d(\gamma mc^2)}{dt} = -e\vec{v} \cdot \vec{E}. \quad (2.5)$$

If the electron velocity is defined by  $\vec{v} = \vec{\beta}c$ , then the Lorentz force equation, (2.4), becomes:

$$\frac{d(\gamma\vec{\beta})}{dt} = -\frac{e}{mc}(\vec{E} + \vec{\beta} \times \vec{B}), \quad (2.6)$$

and the energy equation takes on the form of Equation (2.1). An electron's motion will be described by its six state-space coordinates  $(\vec{x}(t), \dot{\vec{x}}(t))$ . The force and energy equations form a system of six equations the solutions of which will yield the state space coordinates. The Lorentz factor equation,  $\gamma^2 = 1 - \vec{\beta} \cdot \vec{\beta}$  gives a seventh equation. It is sufficient to reduce these to a system of five equations and four unknowns,  $(\vec{x}(t), \gamma(t))$ . The force on an electron due to the circularly-polarized electromagnetic wave and the undulator magnetic field is:

$$\frac{d(\gamma\vec{\beta}_\perp)}{dt} = -\frac{e}{mc}[E(1 - \beta_z)(\cos\psi, -\sin\psi, 0) + \beta_z B(-\sin(k_o z), \cos(k_o z), 0)], \quad (2.7)$$

and

$$\frac{d(\gamma\beta_z)}{dt} = -\frac{e}{mc}[E(\beta_x \cos\psi - \beta_y \sin\psi) + B(\beta_x \sin(k_0 z) - \beta_y \cos(k_0 z))], \quad (2.8)$$

where  $\vec{\beta}_\perp = (\beta_x, \beta_y)$  is the electron's transverse velocity and  $\beta_z$  is the magnitude of the electron's axial velocity. The electron's energy is given by:

$$\frac{d\gamma}{dt} = -\frac{e}{mc}E[\beta_x \cos\psi - \beta_y \sin\psi]. \quad (2.9)$$

For relativistic electrons,  $E(1 - \beta_z) \ll B\beta_z$ , so that Equation (2.7) becomes:

$$\frac{d(\gamma\vec{\beta}_\perp)}{dt} \approx -\frac{e}{mc}[\beta_z B(-\sin(k_0 z), \cos(k_0 z), 0)], \quad (2.10)$$

which can be integrated and a closed form solution found for  $\vec{\beta}_\perp$ :

$$\vec{\beta}_\perp \approx -\frac{K}{\gamma}(\cos(k_0 z), \sin(k_0 z), 0), \quad (2.11)$$

where  $K = eB/k_0 mc^2$  is the undulator parameter. This equation describes periodic motion of the electron in the transverse direction as it travels through the undulator. The constants of integration have been neglected indicating perfect injection of the electron beam into the undulator. An actual electron beam would have some value of emittance, the measure of the beam's radial and angular spread, which would yield non zero constants of integration [1]. The term  $K/\gamma$ , is the amplitude of the transverse periodic motion of the electron as it travels through the undulator magnetic field. When  $K/\gamma \ll 1$ , the transverse deflections are small and have a minor effect on the electron's axial motion. When  $K/\gamma \gg 1$ , the deflections are large and the electron is not energetic enough to make it through the undulator [1]. For the FEL  $K \approx 1$  and  $\gamma \gg 1$  making  $K/\gamma \ll 1$ . By substituting the  $\beta_x$  and  $\beta_y$  solution from Equation (2.11) into the energy equation, (2.9), becomes:

$$\dot{\gamma} = \frac{eE}{mc} \frac{K}{\gamma} \cos(\zeta + \phi), \quad (2.12)$$

where  $\zeta = (k+k_0)z - \omega t$  is the electron phase in the combined undulator and optical fields.  $\zeta$  is a microscopic variable measuring the electron position on the order of  $\lambda$ ,

and describes the phase of the electron motion due to the undulator relative to the phase of the electric field of the optical wave. An electron will have maximum energy transfer to the optical wave when its velocity vector,  $\vec{\beta}_\perp$ , is exactly parallel to the electric field vector of the optical wave or at  $\zeta = \pi$  for an extended time.

The optical wave wavenumber,  $k$ , and the undulator wavenumber  $k_o$  are fixed, assuming single mode operation, so that only  $\zeta(t) \propto z(t)$  evolves as the electron travels through the undulator. At  $t = 0$ , the electron is at the beginning of the undulator,  $\zeta(0) = \zeta_o = (k + k_o)z_o$ . Since  $\lambda \ll \lambda_o$ ,  $\zeta_o \approx kz_o = 2\pi z_o/\lambda$ , the electrons will have a nearly uniform distribution of phases across an optical wavelength initially. As the electrons evolve during transit through the undulator about half will gain energy and about half will lose energy. Assuming  $N \gg 1$ , the efficiency of the undulator is low and  $\gamma$  can be removed as a dynamical variable [1]. Using the Lorentz factor equation, the change in energy,  $\dot{\gamma}/\gamma$  can be related to the change in axial speed,  $\beta_z$ :

$$\gamma^{-2} = 1 - \beta_z^2 - \beta_\perp^2, \quad (2.13)$$

which on substitution of  $\beta_\perp$ , Equation (2.11), becomes:

$$1 - \beta_z^2 = (1 + K^2) \gamma^{-2}. \quad (2.14)$$

The rate of change of the electron energy,  $\dot{\gamma}$ , is given by the time derivative of Equation (2.14). The rate of change of the fractional energy is:

$$\frac{\dot{\gamma}}{\gamma} = \frac{\gamma^2 \beta_z \dot{\beta}_z}{(1 + K^2)}, \quad (2.15)$$

where  $\dot{\beta}_z$  is the axial acceleration. The axial acceleration is related to  $\zeta$  by:

$$\dot{\beta}_z = \frac{\ddot{\zeta}}{(k + k_o)c}, \quad (2.16)$$

where  $\ddot{\zeta}$  is the electron phase "acceleration" and describes the phase dynamics. Combining the resonance condition  $\lambda = \lambda_o/2\gamma^2$ ,  $\dot{\beta}_z$ , Equation (2.16), and  $\dot{\gamma}/\gamma$ , Equation (2.15), yields the pendulum equation:

$$\ddot{\zeta} = \frac{2k_o eKE}{\gamma^2 m} \cos(\zeta + \phi) . \quad (2.17)$$

An average electron will travel through the undulator in a time  $\Delta t = L/\beta_o c$ . The bunching of the electrons is on the order of the optical wavelength  $\lambda \ll L$ . Therefore, all of the electrons take approximately the same amount of time to travel through the undulator. An electron's time in the undulator relative to the total time to travel through the undulator will be given by:

$$\tau = \frac{\beta_o ct}{L} \approx \frac{ct}{L} , \quad (2.18)$$

where  $\tau$  is the dimensionless time, and  $\tau = 0$  and  $\tau = 1$  at the beginning and end of the undulator respectively. The derivative with respect to  $\tau$  will be related to the time derivative by  $(\dot{\phantom{x}}) = d(\phantom{x})/d\tau = (L/c) d(\phantom{x})/dt$ . The pendulum equation becomes:

$$\ddot{\zeta} = \dot{v} = |a| \cos(\zeta + \phi) , \quad (2.19)$$

where  $|a| = 4\pi NeKLE/\gamma^2 mc^2$  is the magnitude of the dimensionless optical field amplitude and  $v = \dot{\zeta}$  is the phase velocity. The pendulum equation, (2.19), describes the phase dynamics of the electron relative to the optical wave. The motion is similar to that of a pendulum. In phase space,  $(\zeta, v)$ , the motion will be described by open and closed orbits dependent on the electron initial energy and the dimensionless field amplitude,  $a$ . The dimensionless field amplitude will define the separatrix, i.e., the locus of points on the threshold between the open and closed orbits defined by the pendulum equation, and is proportional to the magnitude of the optical wave electric field [1].

If the number of undulator periods is low,  $N \geq 1$ , the undulator is more efficient and the change of an electron's energy as it passes through an undulator period will be larger, since  $\Delta\gamma \propto 1/N$ . With low  $N$ , the change in  $\gamma$  as the electron moves through an undulator period must be taken into account in the derivation of the pendulum equation, (2.19). Although the derivation is essentially the same, a slightly different form of the pendulum equation is obtained [8]. For low  $N$  the pendulum equation

becomes:

$$\zeta^{\infty} = (1 - 3v/4\pi N) |a| \cos(\zeta + \phi) . \quad (2.19a)$$

This more general form of the pendulum equation takes into account the change in electron phase due to the electron's energy change as it passes through an undulator period. As  $N$  becomes large, Equation (2.19a) reduces to the pendulum equation, (2.19). A detailed derivation of Equation (2.19a) is given in Reference [8].

### C. THE OPTICAL WAVE EQUATION

In the FEL oscillator spontaneous emission rapidly forms a classical electromagnetic wave [1]. In the FEL amplifier the wave is established by an external source. Once established the evolution of the optical wave can then be described by Maxwell's equations. The fields can be derived from the vector potential  $\vec{A}(\vec{x}, t)$  [7]. The wave equation for the optical wave is:

$$\nabla^2 \vec{A} - \frac{1}{c^2} \frac{\partial^2 \vec{A}}{\partial t^2} = - \frac{4\pi}{c} \vec{J}_{\perp} , \quad (2.20)$$

where  $\vec{J}_{\perp}(\vec{x}, t)$  is the transverse component of the current density. The total current density will be the summation of the individual particle currents:

$$\vec{J}_{\perp} = \sum_i \vec{J}_{\perp i} = -ec \sum_i \vec{\beta}_{\perp i} \delta^{(3)}(\vec{x} - \vec{r}_i) , \quad (2.21)$$

where  $\vec{r}_i$  is the trajectory of the  $i^{th}$  particle. It is the transverse current density which couples the electron beam to the optical wave.

The wave equation can be simplified if the character of the electromagnetic field is considered. The fields in the undulator are those given by Equation (2.3). In order to maintain optical coherence the spatial and temporal variance of the field amplitude,  $E(z, t)$ , must be small over several optical wavelengths. If this were not the case, the laser would have a broadband spectrum. Therefore, the field envelope varies slowly over one optical period, ( $\dot{E} \ll \omega E, \dot{\phi} \ll \omega \phi$ ), and one optical wavelength,



( $E' \ll kE$ ,  $\phi' \ll k\phi$ ). Thus any terms involving second-order derivatives or combinations of derivatives are minor and may be neglected. The fields describing such an optical wave can be derived from the vector potential:

$$\vec{A}(\vec{x}, t) = \frac{E(z, t)}{k} [\sin(\psi), \cos(\psi), 0]. \quad (2.22)$$

The derivation is also simplified if the fields are defined by two rotating unit vectors along the direction of the electric and magnetic fields,  $\hat{e}_1 = \vec{E}_s/E$  and  $\hat{e}_2 = \vec{B}_s/E$ . The wave equation becomes:

$$2 \left[ \frac{\partial E}{\partial z} + \frac{1}{c} \frac{\partial E}{\partial t} \right] \hat{e}_1 - 2E \left[ \frac{\partial \phi}{\partial z} + \frac{1}{c} \frac{\partial \phi}{\partial t} \right] \hat{e}_2 = -\frac{4\pi}{c} \vec{J}_\perp(\vec{x}, t). \quad (2.23)$$

The transverse force on the electron from the radiation field is minute. Therefore, the transverse velocity  $\vec{\beta}_\perp$  is due mainly to the undulator field [9]. Projecting the current density onto the two unit vectors  $\hat{e}_1$  and  $\hat{e}_2$ :

$$\vec{J}_\perp \cdot \hat{e}_1 = \frac{eck}{\gamma} \cos(\zeta + \phi) \delta^{(3)}(\vec{x} - \vec{r}_i), \quad (2.24)$$

and

$$\vec{J}_\perp \cdot \hat{e}_2 = \frac{eck}{\gamma} \sin(\zeta + \phi) \delta^{(3)}(\vec{x} - \vec{r}_i), \quad (2.25)$$

where  $\zeta$  is the solution to pendulum equation derived earlier. The wave equation becomes two scalar first order differential equations:

$$\left[ \frac{\partial E}{\partial z} + \frac{1}{c} \frac{\partial E}{\partial t} \right] = -\frac{2\pi ek}{\gamma} \cos(\zeta + \phi) \delta^{(3)}(\vec{x} - \vec{r}_i), \quad (2.26a)$$

$$E \left[ \frac{\partial \phi}{\partial z} + \frac{1}{c} \frac{\partial \phi}{\partial t} \right] = \frac{2\pi ek}{\gamma} \sin(\zeta + \phi) \delta^{(3)}(\vec{x} - \vec{r}_i). \quad (2.26b)$$

Within a small volume  $dV$ , at a given time, the spatial variance of the optical field amplitude and phase is small. Also, the bunching of the electrons on the order of an optical wavelength does not destroy the macroscopic electron pulse shape nor affect

the average particle density of the pulse [9]. By averaging the wave equation over a volume  $dV$  and several optical wavelengths long, the spatial change of the optical field amplitude and phase can be neglected and the current density made a spatial average of the electrons weighted to the electron particle density,  $\rho_{<...>}$ . The wave equation becomes:

$$\frac{1}{c} \frac{\partial E}{\partial t} = -\frac{2\pi e K \rho}{\gamma} \langle \cos(\zeta + \phi) \rangle, \quad (2.27a)$$

$$E \frac{1}{c} \frac{\partial \phi}{\partial t} = \frac{2\pi e K \rho}{\gamma} \langle \sin(\zeta + \phi) \rangle. \quad (2.27b)$$

Defining these equations in terms of the dimensionless field amplitude  $a$  and the dimensionless time  $\tau$  we have,

$$\dot{|a|} = -j \langle \cos(\zeta + \phi) \rangle, \quad (2.28a)$$

$$\dot{\phi} = \frac{j}{|a|} \langle \sin(\zeta + \phi) \rangle, \quad (2.28b)$$

where  $j = 8N(e\pi K L)^2 \rho / \gamma^3 m c^2$  is the dimensionless current density. These two equations can be replaced by a single equation of a complex variable:

$$\dot{a} = -j \langle e^{-i\zeta} \rangle \quad (2.29)$$

where  $a = |a| e^{i\phi}$  is the complex dimensionless field amplitude. From these equations, the effects of electron bunching are noticeable. Electrons bunching at the phase  $(\zeta + \phi) = \pi$  drive the optical amplitude, while electrons bunching at the phase  $(\zeta + \phi) = \pi/2$  drive the optical phase. Increasing the beam current increases  $j$  and results in larger changes in the amplitude or the phase of the optical wave for a given bunching of the phase,  $\zeta$ .

As with the derivation of the pendulum equation, (2.19), the derivation of the dimensionless optical wave equation, (2.29) assumes that the efficiency of the undulator is not large,  $N \gg 1$  [1]. The change in the electron dynamics in an efficient undulator, low  $N$ , modifies the pendulum equation, (2.19) so that it takes the form of Equation (2.19a) [8]. The modified electron dynamics affect the optical wave via the

self-consistent Lorentz factor,  $\gamma^{-1} \approx (1 - v/4\pi N)\gamma_0^{-1}$  [8]. In a low  $N$  undulator the electron energy is dependent on the phase,  $\zeta$ , and must be included in the phase average. This results in a modified optical wave equation given by:

$$\ddot{a} = j \langle (1 - v/4\pi N) e^{-i\zeta} \rangle. \quad (2.29a)$$

This form of the dimensionless optical wave equation accounts for the energy change of the electrons as they pass through a period of an efficient undulator and is a more general form. For large  $N$ , Equation (2.29a) takes on the form of the dimensionless optical wave equation, (2.29). A detailed derivation of Equation (2.29a) is given in Reference [8].

#### D. THE LOW CURRENT LOW GAIN FEL

The pendulum equation, (2.19) and the dimensionless optical wave equation, (2.29) form a self-consistent Maxwell-Lorentz theory of the FEL [1]. The self-consistency arises from the changes forced on the electron pulse by the optical wave via the Lorentz force which in turn effect changes on the optical wave via Maxwell's equations. The dimensionless current density  $j$  couples the electron beam to the optical wave and determines the magnitude of change to the optical field. Both the wave and pendulum equations are valid for strong ( $a \geq \pi$ ), or weak fields ( $a \leq \pi$ ), and high ( $j \geq \pi$ ), or low current ( $j \leq \pi$ ).

When the current density is low,  $j \leq \pi$ , the complex optical field amplitude,  $a$ , remains essentially constant as the electrons evolve through the undulator. This simplifies the integration of the pendulum equation. The evolution of the electrons in phase space can be examined in order to determine how the electrons bunch as they travel through the undulator. The change in electron phase with respect to the relative time spent in the undulator will be given by:

$$v = \frac{d\zeta}{d\tau} = L[(k + k_0)\beta_z - k]. \quad (2.30)$$

$v$  is the phase velocity and describes the rate at which an electron changes phase. The initial phase velocity,  $v_o$ , of an electron represents the difference between the frequency with which the electron passes through the periodic field of the undulator, and the frequency at which the optical wavelengths pass over the electrons [1]. At resonance the frequencies are equal, and  $v_o = 0$ . Near resonance, small changes in the phase velocity can be related to the change in the electron energy by:

$$\delta v = 4\pi N \frac{\delta \gamma}{\gamma} . \quad (2.31)$$

Rewriting the pendulum equation in terms of the phase velocity:

$$\dot{v} = |a| \cos(\zeta + \phi) , \quad (2.32)$$

which in the low gain limit can be integrated to a closed form solution:

$$v^2 = 2|a| \sin(\zeta + \phi) + 2H_o , \quad (2.33)$$

where  $H_o$  is a constant of the motion resulting from the conservation of energy.  $H_o$  determines the specific phase-space path for an electron with a given  $(\zeta_o, v_o)$  [1].

The evolution of the electrons in phase space can yield particular insight into the operation of the FEL. The phase space points  $(-\pi/2, 0)$  and  $(3\pi/2, 0)$  are fixed and unstable and correspond to a pendulum at the top of its arc. The phase space point  $(\pi/2, 0)$  is fixed and stable and corresponds to a pendulum at the bottom of its arc. The points near  $(\pi, v)$  transfer energy to the optical wave, while the points near  $(0, v)$  transfer energy to the electrons. When the coherence length of the optical wave is long, one  $2\pi$  section of the phase space is adequate to represent others nearby, and corresponds to a section in the electron beam approximately one optical wavelength long [1]. The phase space paths of the electrons will either be open or closed depending on their initial phase and phase velocity,  $(\zeta_o, v_o)$ , and the magnitude of the dimensionless field strength  $|a|$ . The separatrix separates the open orbits from the closed orbits. The points along the separatrix correspond to a pendulum which has just enough energy to make it to the top of its arc, the phase space point  $(3\pi/2, 0)$  or

$(-\pi/2, 0)$ . The separatrix is derived from equation (2.33) and is given by:

$$v_s^2 = 2|a| \sin(\zeta_s + \phi) . \quad (2.33a)$$

The peak-to-peak height of the separatrix is  $4\sqrt{|a|}$ . An electron starting with  $v_o > v_s$  will traverse phase space on an open orbit. This would correspond to a pendulum with enough angular momentum to swing completely around its arc. The phase space evolution of electrons through a weak field, ( $a_o = \pi$ ) low gain, ( $j = 1$ ), undulator is shown in Figure 4. The electrons are injected into the undulator with uniformly spaced phases between  $\zeta = -\pi/2$  and  $\zeta = 3\pi/2$ , the phase velocity for maximum gain,  $v_o = 2.6$ , and a random phase velocity spread of  $\sigma_G = 0.1$ . The starting positions of the electrons is light grey with the paths of the electrons getting darker as the end of the undulator is approached. The final positions of the electrons is shown as black dots. The separatrix is shown as two curves connecting the unstable fixed points of  $(-\pi/2, 0)$  and  $(3\pi/2, 0)$ . The figure was generated by numerically solving the pendulum equation, (2.19), and the optical wave equation, (2.29). The electrons with initial conditions,  $(\zeta_o, v_o)$ , above the separatrix follow open orbits along the separatrix. Those electrons with  $(\zeta_o, v_o)$  below the separatrix follow closed orbits around the stable fixed point  $(\pi/2, 0)$ . The electrons bunch near the phase,  $\zeta \approx \pi$ . Also plotted is the gain  $G$  and optical phase,  $\phi$  with respect to  $\tau$ .

In the low gain limit with weak fields, ( $a < \pi$ ), a solution of the pendulum equation as a function of  $\tau$  can also be obtained by using a perturbation theory and expanding near  $(\zeta_o, v_o)$ . A phase average is then obtained by summing over all  $\zeta_o$ . The average phase velocity is:

$$\langle v \rangle = \langle v^{(0)} \rangle + \langle v^{(1)} \rangle + \langle v^{(2)} \rangle + \dots , \quad (2.34)$$

where  $\langle \dots \rangle = \int_0^{2\pi} (\dots) d\zeta_o / 2\pi$  indicates the phase average, and  $v^{(n)}$  is the  $n^{th}$  order perturbation solution. The zeroth-order solution will be the initial electron phase velocity  $v_o$ . To first order, the same number of electrons gain energy as lose energy

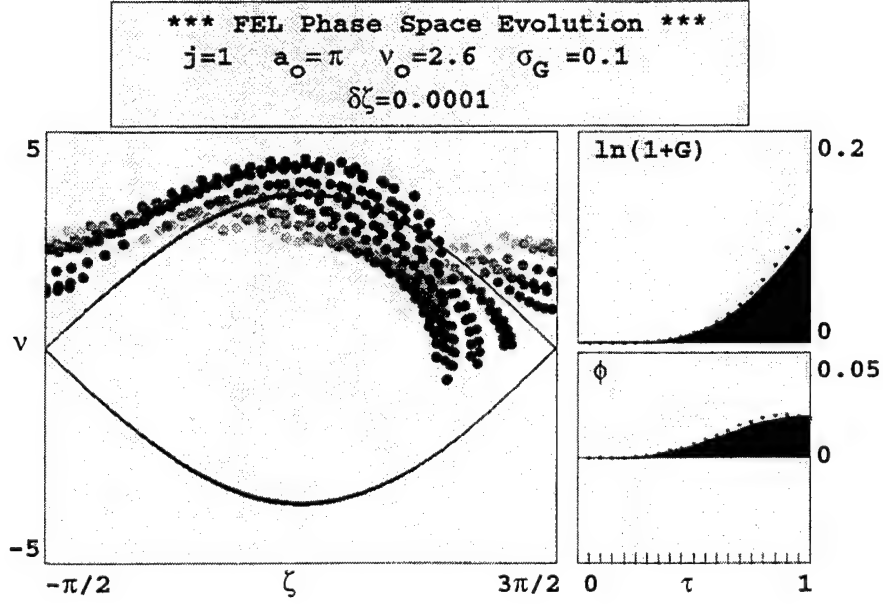


Figure 4. Electron phase space evolution with low current and weak fields. Note the bunching of electrons near  $\zeta=\pi$ . From [1].

and  $\langle v^{(1)} \rangle = 0$ . To second order, bunching of the electrons effects the rate of energy transfer to the optical wave. For some values of  $v_o$ , more electrons lose energy than gain and:

$$\langle v^{(2)} \rangle = \frac{a_o^2}{2v_o^3} \left[ 2\cos(v_o\tau) - 2 + v_o\tau \sin(v_o\tau) \right], \quad (2.35)$$

where  $a_o$  is the initial optical field amplitude [1]. The average change in phase velocity of a monoenergetic electron beam will be given by:

$$\langle \Delta v \rangle = \langle v \rangle - v_o \approx \langle v^{(2)} \rangle, \quad (2.36)$$

which can be related to the average change in energy of an electron from Equation (2.31):

$$\Delta \bar{\gamma} mc^2 \approx \gamma mc^2 \frac{\langle v^{(2)} \rangle}{4\pi N}. \quad (2.37)$$

The number of electrons in a volume element  $dV$  is  $\rho dV$ , the energy given to the optical wave in  $dV$  is  $\rho \Delta \bar{\gamma} m c^2 dV$ , and the amount of radiation energy in  $dV$  is  $2E^2 dV / 8\pi$ . Defining gain as,  $G = dP/P$ , the fractional growth in optical power. The gain becomes:

$$G = j \frac{2 - 2\cos(v_o \tau) - v_o \tau \sin(v_o \tau)}{v_o^3} . \quad (2.38)$$

Again  $j$  emerges as the most important FEL parameter. The current density provides the electron beam optical wave coupling and is the parameter that determines the gain. Low current means low gain, high current means high gain.

For small  $\tau$ ,  $G \rightarrow 0$ , hence there is very little gain in the first part of the undulator. As  $\tau$  increases the bunching of the electrons causes the gain to increase. As shown in Figure 4, the increase in gain is very slow near  $\tau = 0$ . For small  $\tau$ ,  $G \approx j v_o \tau^4$  [1]. The gain is also dependent on the initial phase velocity  $v_o$ . As shown in Figure 5, the gain is anti-symmetric with respect to  $v_o$ . Also shown in Figure 5 is the phase as a function of  $v_o$ . For  $v_o < 0$ , there is negative gain. In this case the electrons bunch near  $\zeta = 0$  and absorb energy from the optical wave. When  $v_o > 0$ , the electrons bunch near  $\zeta = \pi$  and give energy to the optical wave. At resonance,  $v_o = 0$ , as many electrons gain energy as lose energy so that the overall gain is zero. However, the electrons bunch near  $\zeta = \pi/2$ . From the solution to the optical wave equation, (2.28), electrons bunching near this phase drive the phase of the optical wave. The peak gain of  $G \approx 0.135j$  occurs at  $v_o \approx 2.6$ .

## E. STRONG OPTICAL FIELDS

During operation, many passes through the undulator are required to build the optical field. In weak fields,  $|a| \ll \pi$ , the open orbit region of the phase space is large. This can be seen from separatrix equation, (2.33a), which is derived from Equation (2.33).  $H_o$  in Equation (2.33) can be considered the total phase energy of the electron with in the undulator and the optical wave. This total energy is given by:

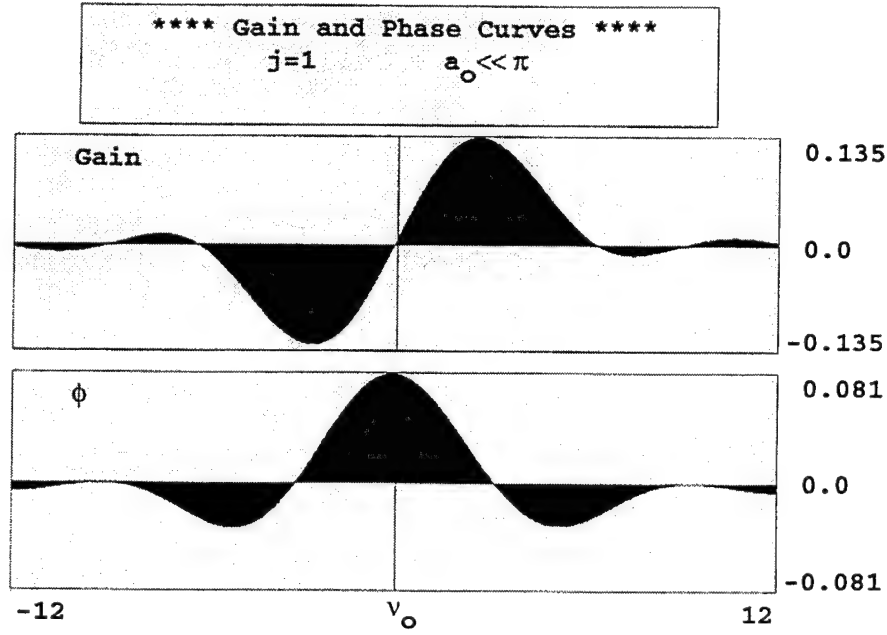


Figure 5. The weak-field gain spectrum  $G(v_o)$ , and phase shift  $\phi(v_o)$  for low current.

$$H_o = \frac{v_o^2}{2} - |a| \sin(\zeta_o + \phi), \quad (2.39)$$

and in the low gain limit is a constant of the motion as the electrons evolve through the undulator. The part of the total energy given by

$$V_{eff} = -|a| \sin(\zeta + \phi) \quad (2.40)$$

can be considered an effective phase potential energy,  $V_{eff}$ , of the optical wave-electron system [10]. The phase potential will have a maximum value of  $|a|$  at the unstable fixed points and  $-|a|$  at the stable fixed point. An electron will follow an open orbit when injected with  $H_o > |a|$ , and will follow a closed orbit when injected with  $-|a| < H_o < |a|$ . In weak fields when the electrons are injected for maximum gain,  $v_o \approx 2.6$ ,  $H_o > |a|$  and the electrons follow open orbits. The electrons acquire a



small energy difference, a small amount of bunching occurs, and the optical field grows. On subsequent passes, the optical field amplitude continues to grow. As  $|a|$  increases, the height of the separatrix increases and the closed-orbit region becomes a larger part of the phase space. Furthermore, the size of the effective potential,  $V_{eff}$ , increases while  $H_0$  decreases. When  $H_0 \leq |a|$ , the electrons near  $\zeta \approx \pi/2$  begin to follow closed orbits. This occurs when  $|a| \geq v_0^2/2$  or when the height of the separatrix,  $2\sqrt{|a|} \geq 2.6$ . As  $|a|$  increases on subsequent passes, more electrons enter the undulator with  $H_0 < |a|$  and follow closed orbits. The stronger fields enhance bunching near  $\zeta \approx \pi$  and increase the efficiency of the energy transfer to the optical wave [1]. The fields remain weak enough that only part of the closed orbit has been traversed and  $v > 0$  as the electrons exit the undulator.

As the optical field amplitude grows stronger, the number of electrons evolving along closed orbital paths increases. The actual paths of the electrons in phase space require solutions of the pendulum equation (2.19) involving elliptic integrals [10]. However, the paths of the electrons near the stable fixed point,  $\zeta \approx \pi/2$ ,  $v \approx 0$  can be approximated by expanding the pendulum equation in a Taylor series around this point. Letting  $\zeta = (\pi/2 + \delta\zeta)$  and  $v \approx \delta\zeta \ll \pi$ , the pendulum equation becomes:

$$\delta\ddot{\zeta} \approx |a| \sin(\delta\zeta + \phi) \approx |a| (\delta\zeta + \phi), \quad (2.41)$$

when  $\delta\zeta + \phi \ll 1$ . The motion of the electrons near the stable fixed point approximates that of a harmonic oscillator with angular frequency  $v_s = \sqrt{|a|}$ , known as the synchrotron frequency. The phase space motion can be seen in Figure 4 for the electrons starting below the separatrix near  $\zeta \approx \pi/2$ .

When  $|a| \geq \pi$ , the optical fields become strong enough to move the electrons from  $v > 0$  to  $v < 0$  prior to the end of the undulator. The electrons that are near  $\zeta \approx \pi$  continue on downward paths in phase space and eventually begin to fall back in  $\zeta$ . The maximum amount of energy lost by the electron bunch is determined by the height of the separatrix,  $4\sqrt{|a|}$ . Once the electrons approach the bottom of their orbits

they no longer lose energy to the optical amplitude, but begin to drive the optical phase. This begins the strong optical field region of operation of the FEL and marks the onset of saturation. The gain no longer follows the small field gain approximation given by Equation (2.38) and now begins to depend on the optical field,  $|a|$  [11]. Further increases in the optical field amplitude cause the electrons originally bunched near  $\zeta \approx \pi$  to continue on their closed path towards  $\zeta = 0$ .

As the optical fields get stronger, ( $|a| \gg \pi$ ), the gain spectrum  $G(\nu_o)$  changes its shape [1]. The spectrum for weak fields and low gain is shown in Figure 5. The spectrum is asymmetric about  $\nu_o = 0$  with the maximum gain at  $\nu_o \approx 2.6$  and the maximum absorption at  $\nu_o \approx -2.6$ . With the stronger optical fields, the amount of time the electrons remain bunched becomes a smaller fraction of  $\tau$  [11]. As a result, the peak gain falls to about 5% of the maximum of  $G = 0.135j$  for weak fields for  $a_o \approx 40$ . Also, the magnitude of  $\nu_o$  corresponding to the peak gain and loss increase. Eventually, the gain per pass equals the loss per pass, and the FEL reaches steady-state saturation.

## F. MODE COMPETITION AND COHERENCE DEVELOPMENT

Thus far, the discussion has assumed the FEL to be operating in a single mode. However, when the FEL oscillator begins operation, there is no electromagnetic field for the electrons to couple with. The radiation produced is that of the oscillating, relativistic electrons as they travel through the undulator. The radiation emitted by relativistic electrons is given by the Liénard-Wiechert potential [12]. The spectrum resulting from the spontaneous emission of the electrons will not be monochromatic, but will be a continuous range of frequencies in a narrow band around the resonant frequency [1]. The frequencies will be related to the phase velocity through the wave number,  $k$ , by  $\nu(k) = L[(k + k_o)\beta_z - k]$ . The minimum spacing between the modes will be roughly  $L\Delta k\gamma^{-2}$ . For the FEL, these conditions will result in a continuum of modes. The spontaneous emission lineshape,  $s(\nu) \propto [\sin(\nu/2)/(\nu/2)]^2$ , is symmetric

and has a width of  $\Delta v \approx 2\pi$  [1]. The coherence length of the initial optical signal will be dependent on the interaction of the individual electrons with the undulator. For the relativistic electrons the initial coherence length will be  $N\lambda$  [1].

As the amplitude of the optical wave grows on subsequent passes there is gain or loss in each mode resulting from the small field gain equation, (2.38). The asymmetric shape of the small field gain will amplify those modes near  $v_o \approx 2.6$  and suppress those modes near  $v_o \approx -2.6$ . The change in the power in each mode per pass,  $P_n = |a(n)|^2$ , will be a function of the the gain per pass,  $G(v)P_n$ , the spontaneous emission per mode  $s(v)$ , and the loss per pass,  $P_n/Q$ , and is given by:

$$\Delta P_n(v) = s(v) + P_n(v) \left[ G(v) - \frac{1}{Q} \right], \quad (2.42)$$

where  $n$  is the pass number,  $1/Q$  is the loss per pass from the resonator and  $Q$  is the resonator quality factor. The mode competition will enhance the coherence of the optical wave and increase its coherence length. After a large number of passes,  $n$ ,  $P(v) \gg s(v)$  the power in these modes can be approximated by:

$$P(v,n) \approx P_o e^{\left[ G(v) - \frac{1}{Q} \right] n}. \quad (2.43)$$

By expanding  $P(v,n)$  in a Taylor's series around  $v_o$  at its the maximum gives an approximation of the development of each mode. The final spectrum will be centered around this phase velocity and be a function of the second derivative of  $G(v)$ . This approximation gives an optical spectrum of  $\Delta v \approx 2\pi(nj)^{-1/2}$  [1]. Since, from the phase velocity equation, (2.30),  $\Delta v \approx \pi N \Delta \lambda / \lambda$ , this corresponds to a shift in the physical optical spectrum of  $\Delta \lambda / \lambda \approx 1/N(nj)^{1/2}$ . The coherence length is given by  $l_c \approx \lambda^2 / \Delta \lambda$  [13]. Therefore, the coherence of the FEL grows by  $l_c \approx N \lambda (nj)^{1/2}$ . Once coherence has developed through mode competition, the maximum coherence length will depend on the length of the electron pulse from the RF source and the quality of the undulator and resonator.

## G. LONGITUDINAL MULTIMODE THEORY

The pendulum equation (2.19) and the optical wave equation (2.29) were derived under the assumption of a single operating mode. However, the FEL will develop a multitude of frequencies in a narrow range around the phase velocity giving maximum gain. These multiple frequencies modulate the optical wave and tend to reduce the coherence length. The modulation will manifest itself as a spatial variance of the optical wave. The coherence is maintained over several optical wavelengths so that the assumptions made in deriving the pendulum equation and the optical wave equation remain valid [14]. However, in order to examine the spatial mode development a distance greater than optical wavelength should be used.

Since the relativistic electrons travel at a speed somewhat less than the speed of light, they fall back relative to their starting point on the optical wave. This distance is given by  $L(1 - \beta_z) = N\lambda_o(1 - \beta_z)$ . At resonance  $\lambda_o(1 - \beta_z) \approx \lambda$ , and an electron passes through one undulator period for each wavelength of light passing over it. By the end of the undulator the electron has slipped back by a distance of  $N\lambda$  from its starting point on the optical wave. The slippage process allows one point on the optical wave to communicate to other points, via the electrons, and establishes the long range coherence in the optical envelope [14]. The slippage distance gives a unique scale length to observe development of the modes. By scaling the longitudinal distance to the slippage distance,  $z \rightarrow Z/N\lambda$ , the electrons will change a dimensionless longitudinal distance of  $\Delta z = 1$  during a dimensionless interaction time of  $\tau = 0$  to  $\tau = 1$ . A finite distance that is an integral number of slippage distances can be used to observe the spatial mode development. The optical wave remains stationary and the electrons enter the optical window from the right and exit to the left. For long pulse lengths, the boundary conditions are assumed to be periodic. The number of optical sites used for analysis is dependent upon the amount of detail needed to observe the mode development [1]. The window width is,  $W = mN\lambda/N\lambda = N_w\Delta z$ , where  $m$  is an integer,  $N_w$  is the number of optical sites, and

$\Delta z$  is the spacing between each site.

The pendulum equation (2.19) and the optical wave equation (2.29) become functions of the dimensionless longitudinal distance,  $z$ :

$$\overset{\circ}{v}(z + \tau, \tau) = \overset{\circ}{\zeta}(z + \tau, \tau) = |a(z, \tau)| \cos(\overset{\circ}{\zeta}(z + \tau, \tau) + \phi(z, \tau)) , \quad (2.44)$$

and

$$\overset{\circ}{a}(z, \tau) = j \langle e^{-i\overset{\circ}{\zeta}(z + \tau, \tau)} \rangle . \quad (2.45)$$

The electron phase,  $\zeta$ , becomes a function of  $(z + \tau, \tau)$  in order to account for their slippage past the optical sites. These equations now govern the self-consistent multimode evolution of the electron beam and the optical wave in the undulator [14]. Once the spatial modes of the optical wave are known from  $a(z)$  the longitudinal wavenumbers can be found by taking the spatial Fourier Transform to find  $a(k)$ .

## H. TRAPPED-PARTICLE INSTABILITY

When the dimensionless field amplitude grows to levels approaching,  $|a| \approx 4\pi^2$ , the effective potential,  $V_{eff}$  becomes deep and many electrons are trapped in closed orbits. The electrons near the stable fixed point,  $\zeta_o + \phi \approx \pi/2$ , have a synchrotron frequency,  $v_s = \sqrt{|a|} \approx 2\pi$ , and complete about one full synchrotron oscillation by the end of the undulator. As the electrons carry out these longitudinal oscillations they move from a phase which results in transfer of energy to the optical wave ( $\zeta \approx \pi$ ) to a phase which results in absorption of energy from the optical wave, ( $\zeta \approx 0$ ). The electrons also slip back relative to the optical wave by the slippage distance,  $N\lambda$ , so that the site that receives amplification from a given bunch of electrons may later receive attenuation from a different bunch of electrons slipping back. If the electrons were truly uniform across the wave front and the FEL operated in a single mode, all longitudinal sites would evolve identically and no effect would be observed. However, small differences in the optical field and the number of electrons at each site due to quantum fluctuations, shot noise, etc, can cause the sites to evolve differently. The

optical wave does not consist of a single mode but of multiple modes in a narrow range around some phase velocity,  $v_o$ , giving peak gain at saturation. If there is spatial modulation of the optical wave with a spatial period approximately equal to the slippage distance, the electrons see a time-varying optical wave with a temporal period approximately equal to that corresponding to the synchrotron frequency. The optical wave and electron beam can couple at the synchrotron frequency and cause the pre-existing modulation to grow [15]. The weaker sites of the optical wave are made more weak as electrons evolving from the stronger optical wave sites begin absorbing energy from the optical wave as they slip back into the weaker region. The effect is known as the synchrotron or trapped particle instability [15].

The result is growth of sidebands in the optical wave spectrum at frequencies corresponding to the synchrotron frequency,  $v_s$ . The sidebands appear in the  $a(v)$  spectrum at  $v_o \pm v_s$  corresponding to a physical shift of  $\Delta\lambda/\lambda \approx v_s/2\pi N$ . The range of synchrotron frequencies around  $v_s$  is approximately  $2\pi$  [15]. Since there is a range of synchrotron frequencies, the nonlinearities in the pendulum equation (2.19) and the optical wave equation (2.29) can cause the modulation to also grow at the harmonics of the synchrotron frequency. The effect of the trapped-particle instability is to shift power from the carrier wave into the sideband. The power increase in the sideband causes the steady-state power of the FEL increase. The locally stronger optical fields in the modulated wave result in more efficient extraction of energy from the electrons. However, the coherence of the optical wave has been modified in the strong fields, and will reduce the coherence established by the weak fields. Stronger fields can result from a low loss resonator,  $Q \gg 1$ , or higher current,  $j \gg 1$ .

Figures 6a and 6b show the results of a multimode analysis of the longitudinal evolution of the optical wave. The results are from a numerical simulation using the longitudinal multimode and Maxwell-Lorentz theory. The left plot shows the dimensionless field amplitude,  $|a(z, n)|$ , as a function of  $z$  over a number of passes  $n$ . The shading indicates the relative strengths of the optical field amplitude with the

darker areas corresponding to the weakest field amplitude and the lighter areas corresponding to the stronger fields. The maximum field amplitude,  $|a| =$  is given on the scale above the upper left plot. The upper left plot is the shape of the optical pulse over the window length for the final pass. The middle window is the power spectrum  $P(v, n)$  over the passes. The shading scheme is the similar to the first window with the shading indicating relative power. The upper middle window is the power spectrum on the final pass. The triangular and rectangular tic marks indicate the central wavelength at resonance and center of the spectrum, respectively. The window on the right is a plot of the electron phase velocity distribution,  $f(v, n)$ , over the passes. The shading scheme is similar to the previous windows with the shading indicating relative density of electrons. The uppermost right window is a plot of the phase velocity distribution on the final pass. The triangular and rectangular tic marks indicate the initial phase velocity at resonance and the center of the spectrum, respectively. The three plots across the bottom are, from left to right, the gain at the end of each pass,  $G(n)$ , the weak field gain spectrum, and the power at the end of each pass,  $P(n)$ . The power,  $P(n)$  is found by taking the average value of  $|a(z)|^2$  over all sites in the window. Each figure looks at a window width of four slippage lengths,  $m = 4$  and the evolution of the optical pulse over 1000 passes. The noise is simulated by inserting a random phase displacement for each electron with rms spread  $\delta\zeta = 10^{-4}$ .

In Figure 6a, the combination of  $j = 6$  and  $Q = 5$  are such that the dimensionless field amplitude,  $|a(z)| \approx 16 < 4\pi^2$ , at steady-state never reaches levels high enough to cause appreciable synchrotron motion. This results in a relatively featureless, plot since there is no modulation and all points on the optical wave have approximately the same amplitude. The optical wave amplitude is constant throughout the upper left window,  $a(z, n)$ , indicating single mode operation. This is also shown by the power spectrum,  $P(v, n)$ , by a single peak around the frequency giving peak gain. The power,  $P(n)$  builds up rapidly in a few passes to its steady state-value of  $P(n) = 260$ .

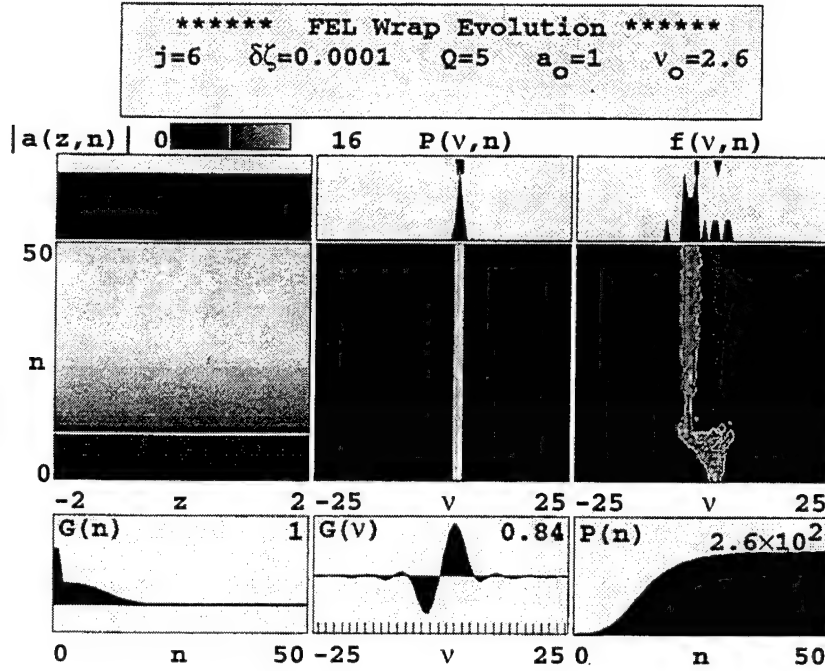


Figure 6a. Longitudinal mode development for  $j = 6$  and  $Q = 5$ .

The gain,  $G(n)$ , peaks in the first few passes then decreases to its steady state value at saturation. The electron phase velocity distribution,  $f(v, n)$  moves to a value less than the initial phase velocity and acquires a small spread indicating transfer of energy to the optical wave.

In Figure 6b, the combination of  $j = 6$  and  $Q = 7$  are such that the dimensionless field amplitude builds to a strength resulting in approximately one-half synchrotron oscillation per pass. The synchrotron frequency is built up from noise over hundreds of passes so that only a fraction of an oscillation is sufficient to transfer information between the sites [1]. The plot of the dimensionless field amplitude  $|a(z, n)|$  shows that the FEL builds to single-mode saturation quickly then remains essentially constant until around  $n \approx 500$ . Then the modulation has formed sites with local field amplitudes great enough to cause approximately one full synchrotron oscillation. The modulation then rapidly builds so that within another 100 passes the modulation is fully



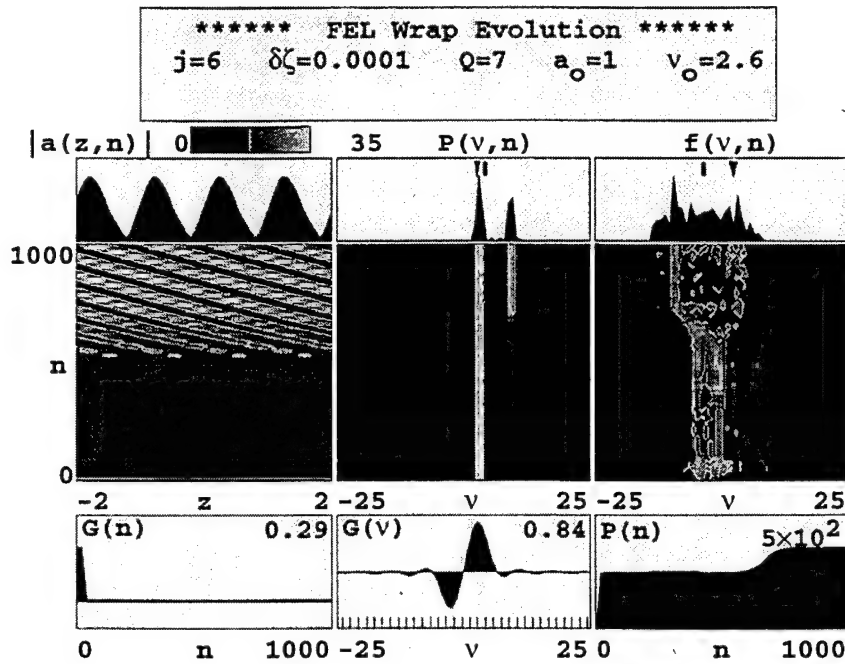


Figure 6b. Longitudinal mode development for  $j = 6$  and  $Q = 7$ .

established. The dimensionless power spectrum,  $P(v, n)$ , shows the growth of a sideband at  $\Delta v \approx v_s = 2\pi$ . The dimensionless power,  $P(n)$ , rises to its single mode steady state value in the first few passes then rises again when the modulation is established indicating more energy is being extracted from the electron beam. The phase velocity distribution,  $f(v, n)$ , also shows that once the modulation is established the phase velocity spread, and hence the energy spread, increases indicating a more efficient energy extraction from the electrons. Figure 7b also shows that the modulation continually moves back in the window. This occurs because the gain is very small in the first part of the undulator, therefore the site of peak amplification slips back each pass. This gives the appearance of the optical wave continually slipping back.

The trapped-particle instability can be a benefit or a problem for operation of the FEL. In situations where high total power is the only concern, the instability can

benefit the user since it results in a more efficient extraction of energy from the electron beam and a higher total output power. However, if the user is concerned with a narrow output spectrum the instability is a problem.

### III. LIMIT-CYCLE BEHAVIOR

#### A. SHORT PULSE THEORY

Up to this point the electron pulse has been assumed to be many slippage distances long. In fact, the pulse length will be determined by the electron source and acceleration method. An RF accelerator produces a train of pulses as opposed to a continuous beam of electrons. The first operable FEL at Stanford used a pulse length of approximately 1 mm [16]. Many FEL oscillators in use today have pulse lengths on the same order [1]. When the pulse length,  $l_e$ , becomes on the order of the slippage distance,  $N\lambda$ , then operation of the FEL becomes subject to a variety of "short pulse effects". These arise because the electrons are subject to a varying optical field as they slip past the optical sites and conversely, the optical wave is subject to a varying density of electrons as it slips forward over the electron pulse sites. The longitudinal multimode theory is a useful tool to describe the evolution of the optical pulse. Since the pulse length is on the order of the slippage distance, there is no need to use periodic boundary conditions and the evolution of the pulse can be followed as a whole. Again, all microscopic longitudinal distances are still normalized to the slippage distance, giving a normalized pulse length of  $\sigma_z = l_e/N\lambda$ .

One of the most prominent effects resulting from short electron pulses in an FEL oscillator is known as "gain lethargy" [16]. The optical wave develops from spontaneous emission by bouncing the emitted light between resonator mirrors separated by a distance,  $S > L$ . An optical pulse starting at the beginning of the undulator will return to its starting point in a time,  $t = 2S/c$ . One would think injection of the sequence of electron pulses should be based on this time to overlap the copropagating optical pulses. But, from the weak field gain equation (2.38), very little amplification of the optical wave occurs in the first part of the undulator, and the majority of the amplification occurs towards end of the undulator. However, the

electrons slip behind the optical sites by the slippage distance,  $N\lambda$ , as they travel through the undulator. This results in the majority of the amplification occurring towards the rear of the optical pulse and causes the optical pulse centroid to move at a speed slightly less than  $c$ . If the electron pulses continue to be injected at a frequency exactly equal to  $c/2S$ , very soon the optical pulse falls behind the newly injected electron pulse. Eventually, the coupling between the optical and electron pulses is lost and the optical pulse decays due to resonator losses.

Figure 7 is a numerical simulation using the longitudinal multimode, pulse, and Maxwell-Lorentz theories to model the short pulse effect. The layout of the figure is similar to that of Figure 6. The lower-left plot is of the electron pulse shown at  $\tau = 0$ , dark grey, and  $\tau = 1$ , light grey, for reference. The electron pulse is assumed to be parabolic in shape and described by a dimensionless current,  $j(z) = j(1 - 2z^2/\sigma_z^2)$  for  $|z| < \sigma_z/\sqrt{2}$  and zero elsewhere. For the simulation, the peak dimensionless current density is  $j = 2.5$ , the resonator losses are given by  $Q = 20$ , and the electron pulse length is one slippage distance,  $\sigma_z = 1.0$ . The electrons are given a random phase displacement of  $\delta\zeta = 10^{-4}$  to simulate noise. The electron pulses are injected exactly synchronized with the optical pulse travel time,  $2S/c$ , giving a desynchronism, discussed below, of  $d = 0$ . The optical pulse grows from noise and is initially the width of the electron pulse length plus the slippage distance,  $\sigma_z + 1$ . Once the optical pulse has formed, the electron pulse couples and the optical pulse grows in intensity and narrows. This can be seen in the middle-left plot of  $|a(z, n)|$ . However, due to the lethargy of the gain mechanism, the peak of the optical pulse forms towards its rear on each pass. This can be seen in the plot of  $|a(z, n)|$  as the stronger part of the pulse, the light grey, decreases in  $z$  on each pass. Eventually, the optical pulse is completely decoupled from the electron pulse, at  $n \approx 300$ , and the optical pulse decays back to noise. The power,  $P(n)$ , peaks and then decreases to zero. The FEL fails to operate.

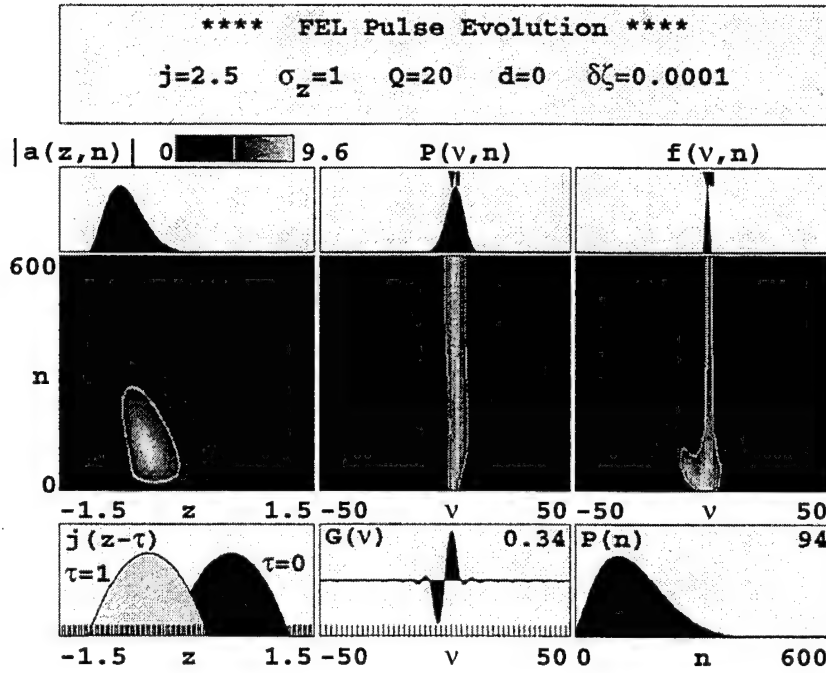


Figure 7. Short Pulse Evolution at exact synchronism.

In order to ensure the optical pulse centroid and the electron pulse are synchronized, the pathlength of the optical pulse must be shortened by a small amount to account for the lethargy of the gain mechanism. The decrease in the pathlength is normally accomplished by moving one of the resonator mirrors by a small amount ( $\approx 5 \rightarrow 10 \mu\text{m}$ ) and is known as desynchronism,  $d$ . The desynchronism is given by:

$$d \approx - \frac{2\Delta S}{N\lambda} \quad (3.1)$$

where  $\Delta S$  is the decrease in the distance between the resonator mirrors. The desynchronism is the distance change normalized to the slippage distance and gives the displacement between the electron and optical pulses at  $\tau = 0$  on each pass [1]. The desynchronism ensures the coupling between the optical and electron pulses is maintained over many passes.

In Figure 7, the desynchronism was  $d = 0$ . Figure 8 is a simulation using the same parameters as Figure 7 but with  $d = 0.003$ . Again the electron pulse is assumed to be parabolic in shape with a peak dimensionless current density,  $j = 2.5$ , the resonator losses given by,  $Q = 20$ , the electron pulse length by  $\sigma_z = 1.0$ , and each electron is given a random phase displacement of  $\delta\zeta = 10^{-4}$ . The optical pulse again grows from noise with a width  $\approx \sigma_z + 1$ . However, the desynchronism advances the optical pulse each pass with the overall effect of maintaining the optical pulse centroid relatively stationary. The optical and electron pulses couple at the beginning of the undulator. The final steady-state optical field amplitude is  $|a| \approx 36$  with power  $P(n) = 173$ . The optical field amplitude is large enough for the trapped particle instability to occur resulting in modulation of the optical pulse and formation of a small sideband.

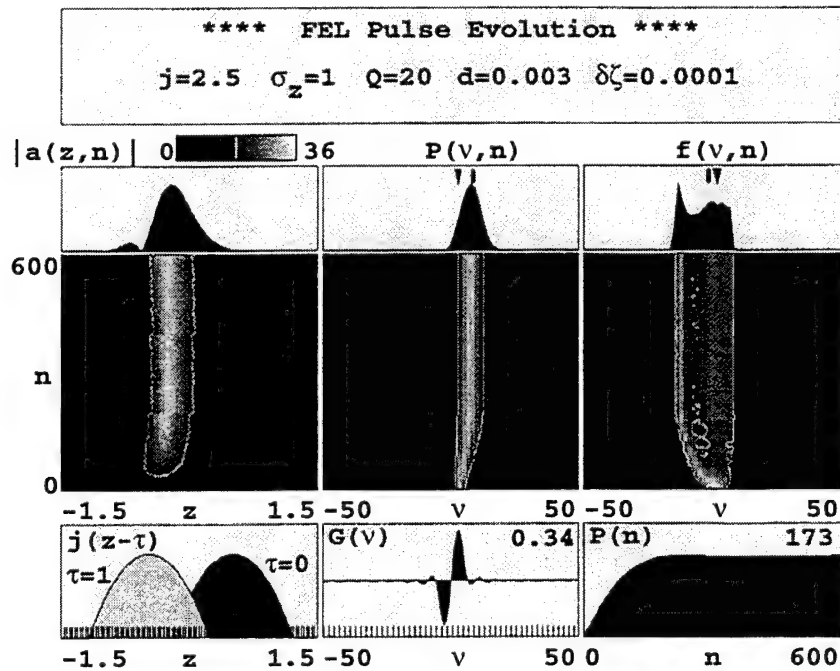


Figure 8. Short pulse evolution with small desynchronism,  $d = 0.001$ .

Desynchronism affects the coupling between the optical and electron pulses increasing the power output of the FEL dramatically. Figure 8 shows that a small change in the desynchronism results in a large change in the operation of the FEL. However, there is only a narrow range over which the desynchronism produces the desired effect. If the desynchronism gets too large, the optical pulse centroid moves ahead of the electron pulse again reducing the optical and electron pulse coupling and reducing the power output of the FEL [16]. The optical pulse becomes wider as  $d$  increases, because the large desynchronism artificially advances the front edge of the optical pulse well ahead of the electron pulse. Only a small fraction of this large optical pulse interacts with the electron pulse and the pulse moves over the electron pulse prior to the end of the undulator. This reduces the coupling between the optical and electron pulses and results in lower optical field amplitudes. The effect of desynchronism on the optical field amplitude can be described by  $|a(z)| \propto \exp(-z/2Qd)$  [1]. Figure 9 shows the relationship between the steady-state power output and desynchronism. The figure is generated from numerical simulations with similar input parameters as those in Figures 7 and 8 varying the values of desynchronism. The curve is asymmetric with a rapid increase of power as the optical path is shortened and the coupling between the optical and electron pulses is enhanced. Eventually, a desynchronism is reached that causes the optical pulse to move ahead of the electron pulse too rapidly, reducing the optical and electron pulse coupling, and causing a reduction of the output power. Experimental observations confirm the general shape of the desynchronism curve [17].

## B. LIMIT-CYCLE BEHAVIOR

The combination of short-pulse effects and the strong optical fields present in the FEL at saturation result in interesting behavior. The combination of the optical and undulator fields result in the trapped-particle instability which cause the electrons trapped near the bottom of the deep potential wells to oscillate at the synchrotron

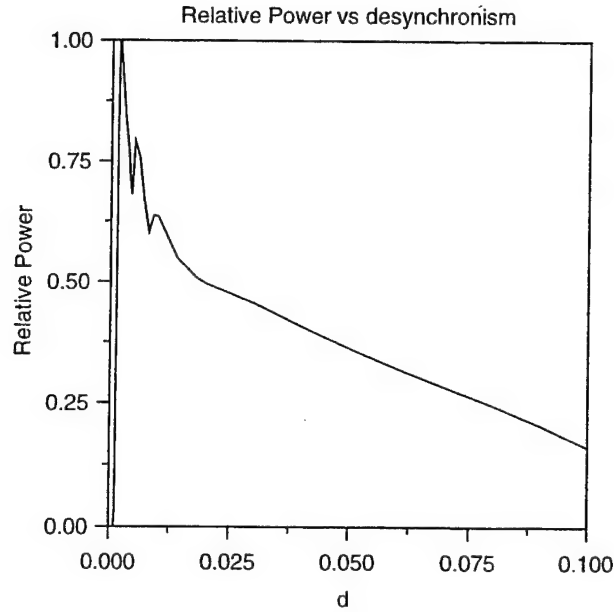


Figure 9. Normalized Power versus desynchronism for  $j = 2.5$ ,  $Q = 30$ , and  $\sigma_z = 1.4$ .

frequency,  $\nu_s = \sqrt{1/a}$ . These oscillations mix with the optical wave causing sidebands at the synchrotron frequency and modulation of the optical wave envelope. This modulation of the short optical pulse combines with the desynchronism mechanism and resonator losses to create an optical pulse that varies in shape and size over many passes. The variance of the pulse size results in a variance of the optical power. The optical pulse also periodically reproduces a given pulse shape over time. The results are a periodic variation of the optical power over time [18].

The pendulum equation (2.19) and the optical wave equation (2.29) resulting from the self-consistent Maxwell-Lorentz theory are inherently nonlinear. Therefore, the FEL operation can best be described by theory which includes nonlinear dynamics. The addition of the desynchronism, resonator losses, and slippage provide damping and create a nonlinear dissipative system in the FEL oscillator [19]. In its simplest



form the dissipative oscillator system reaches a steady-state dependent on the control parameters of  $j$ ,  $Q$ ,  $\sigma_z$ , and  $d$ , where the pulse profile reproduces itself on each successive pass [18]. The FEL operates at a fixed point, or stable solution, and the shape of the optical pulse remains relatively constant with respect to time.

For different values of these control parameters the system can go through a qualitative change in its operation known as a "bifurcation" [20]. The dimension of the bifurcation is determined by the number of parameters controlling the change in the system operation, and is known as a codimension- $n$  bifurcation, where  $n$  is the number of control parameters [20]. A bifurcation which moves the system from a fixed point, or stable solution, to a periodic solution is known as a "Hopf" bifurcation [20]. The control parameters of  $j$ ,  $Q$ ,  $\sigma_z$ , and  $d$  create codimension-four Hopf bifurcation of the FEL oscillator. The bifurcation moves the oscillator from a fixed point solution into a periodic, or limit-cycle solution. The shape of the optical pulse changes with respect to time even though all of the operating parameters of the FEL are constant [18]. In the limit-cycle solution, the optical pulse shape forms, decays, and reproduces itself over successive passes. This results in a periodic oscillation of the power with respect to time. The effect is known as the "limit cycle" behavior, and was first predicted in 1982 [18] and first observed in 1993 [21].

The effect is dependent upon the trapped-particle instability and therefore requires optical field amplitudes large enough to provide significant synchrotron oscillations,  $v_s \geq 2\pi$ , in a slippage distance. The modulation of the optical pulse resulting from the synchrotron frequency forms subpulses in the rear of the optical pulse. While the desynchronism ensures the optical pulse centroid remains relatively stationary with respect to the electron pulse, features in the optical pulse continue to move forward with respect to the optical pulse centroid over many passes. The subpulses formed in the rear of the optical pulse move forward on successive passes into regions of higher gain and grow. As the process continues, the larger subpulses move forward into a region of the optical pulse where there is lower gain and higher

losses causing eventual decay. The optical field amplitude oscillates as this train of subpulses moves through the main pulse and results in oscillations of the optical power even though all operational parameters remain constant. The entire process takes a few hundred passes to complete resulting in power oscillations with periods of the same order.

Figure 10 is a pulse evolution simulation similar to those in Figures 7 and 8. For this simulation,  $j = 2.5$ ,  $Q = 30$ ,  $\sigma_z = 1.4$ , and  $d = 0.01$ . In the upper-left plot,  $a(z)$ , the optical pulse is modulated by the synchrotron frequency and the subpulses are noticeable. The modulation results in a sideband at the synchrotron frequency which is shown in the upper middle plot of  $P(v)$ . In the middle-left plot,  $a(z, n)$ , the subpulses form and march forward as show by the higher intensity, light grey, amplitudes. In the center plot,  $P(v, n)$ , the carrier frequency oscillates as the optical amplitude oscillations result oscillations of the phase velocity resulting in peak gain. In the right- center plot,  $f(v, n)$ , the phase velocity distribution oscillates as the optical amplitude oscillations result in an variation of the energy exchanged per pass. The lower-left and center plots are the electron pulse at  $\tau = 0$  and  $\tau = 1$ , and the weak-field gain spectrum respectively. The limit-cycle behavior is noticeable in the steady-state power  $P(n)$ , the lower-right plot, as an oscillation in the total power over  $n$ .

Figure 11 is a 160 pass "film" over one period of the limit-cycle oscillations in the pulse evolution simulation of Figure 10. The upper three plots,  $a(z, n)$ ,  $P(v, n)$ , and  $f(v, n)$ , are plotted at five intervals over the 160 passes. The lowest three plots are electron pulse position at  $\tau = 0$  and  $\tau = 1$ , the weak-field gain spectrum, and the power,  $P(n)$ , over the interval respectively. A subpulse forms at pass  $n \approx 2575$ , the uppermost plot, moves forward and grows. The larger forward subpulse moves forward and decays as it reaches the front of the optical pulse. The pulse shape at  $n \approx 2735$  is a close reproduction of that at  $n \approx 2575$ . Over this same pass period, the power spectrum  $P(v, n)$  moves to higher and lower values of  $v$ , corresponding physically to a longer and shorter wavelength, as the average optical field amplitude

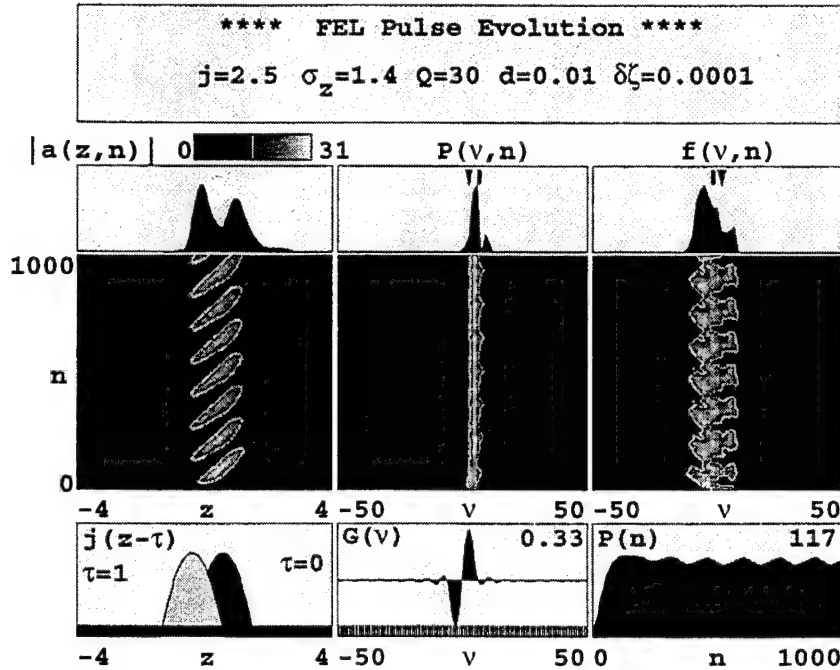


Figure 10. Pulse evolution simulation resulting in limit cycle behavior.

becomes larger and smaller. The sideband at  $v + v_s$  also grows and shrinks in magnitude as the modulation of the optical pulse changes. The phase velocity distribution,  $f(v, n)$  centroid moves between larger and smaller energy extraction, given by the rectangular tic's position relative to the triangular tic. Again, the oscillation is noticeable in the power plot  $P(n)$ , the lower right plot.

The control parameters of  $j$ ,  $Q$ ,  $\sigma_z$ , and  $d$  can result in further bifurcations of the oscillator system which result in quasiperiodic and eventually chaotic behavior. The effect of each control parameter must be examined individually in order to determine its effect on the system. The parameters are not totally independent of each other and each affects the value of a given parameter for which the limit-cycle, quasiperiodic, and chaotic behavior starts. The first bifurcation point occurs when the combination of the parameters result in optical field amplitudes strong enough to cause the trapped-particle instability and drive the carrier wave unstable. The next sections look at the

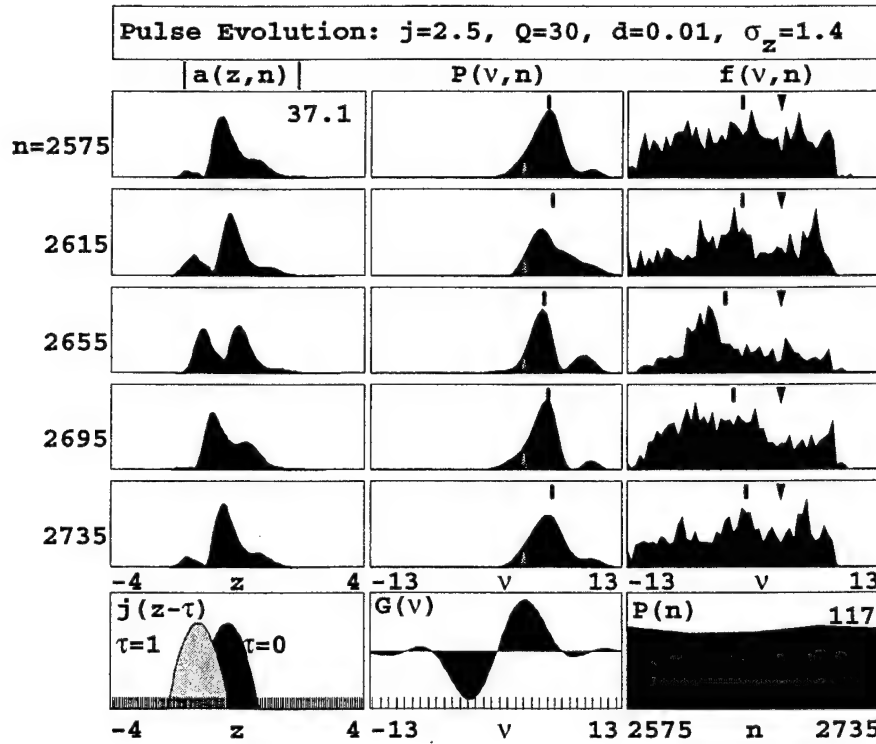


Figure 11. Pulse evolution at various passes during limit cycle operation.

dependence of the oscillator behavior on these parameters and attempt to establish locations of bifurcation points of the quasiperiodic and chaotic behaviors.

### C. EFFECTS OF PHYSICAL CONTROL PARAMETERS

The effects of electron pulse shape on the evolution of the optical pulse shape has been studied extensively [22]. The evolution of the optical pulse over many passes depends on the physical input parameters of  $j$ ,  $Q$ ,  $\sigma_z$ , and  $d$ . Any accurate analytical treatment of the limit-cycle behavior will be dependent on the electron pulse shape, slippage, the complex gain function, resonator losses, and the desynchronization.

## 1. Current Density $j$

As the current density is increased, the steady-state optical field amplitude increases via the gain mechanism. The shape of the optical pulse remains relatively constant as  $j$  is varied until the optical field amplitude reaches strengths sufficient for the trapped-particle instability,  $|a| \geq 4\pi^2$ . At moderate values of  $Q$ , when optical field strengths of this magnitude are reached, the limit-cycle behavior begins [18]. This agrees with Hahn and Lee's finding that the Hopf bifurcation point corresponds to field strengths large enough to cause approximately one synchrotron oscillation in a slippage distance,  $N\lambda$  [19]. Figure 12 is a plot of the amplitude and frequency of the limit-cycle oscillations for various values of  $j$  with  $Q = 30$ ,  $\sigma_z = 1.4$ , and  $d = 0.01$ . The amplitude of the limit-cycle is evaluated as the fractional change of the average power during the cycle. The frequency of the limit-cycle is the fraction of the cycle completed per pass, or the reciprocal of the number of passes required for the limit-cycle to complete one full cycle. The limit-cycle oscillations begin when  $j \geq 1.8$ . As the current density is increased above this value, the size of the oscillations grow and the frequency of the oscillations increases slightly. This is indicative of a stable limit-cycle or periodic solution, since for a small change in the initial conditions the periodic solution remains essentially the same [20].

At  $j \geq 3.4$  the solution passes through a second bifurcation changing the character of the oscillation. The local field strengths within the optical pulse are now large enough to cause more than one synchrotron oscillation per pass. As the optical field increases further, additional frequencies may have gain above threshold so that additional sidebands are formed causing additional modulation of the optical pulse. Figure 13 follows the pulse evolution with  $j = 3.7$ ,  $Q=30$ ,  $\sigma_z = 1.4$  and  $d = 0.01$ . This range of  $j$  results in optical field amplitudes high enough to modulate the optical pulse by more than two subpulses which forms a new sideband at  $\nu_o + 2\nu_s$ . These multiple subpulses no longer reach their maximum at the same  $z$  over time as for the stable limit-cycle case shown in Figure 10. This can be seen in the middle-left plot of

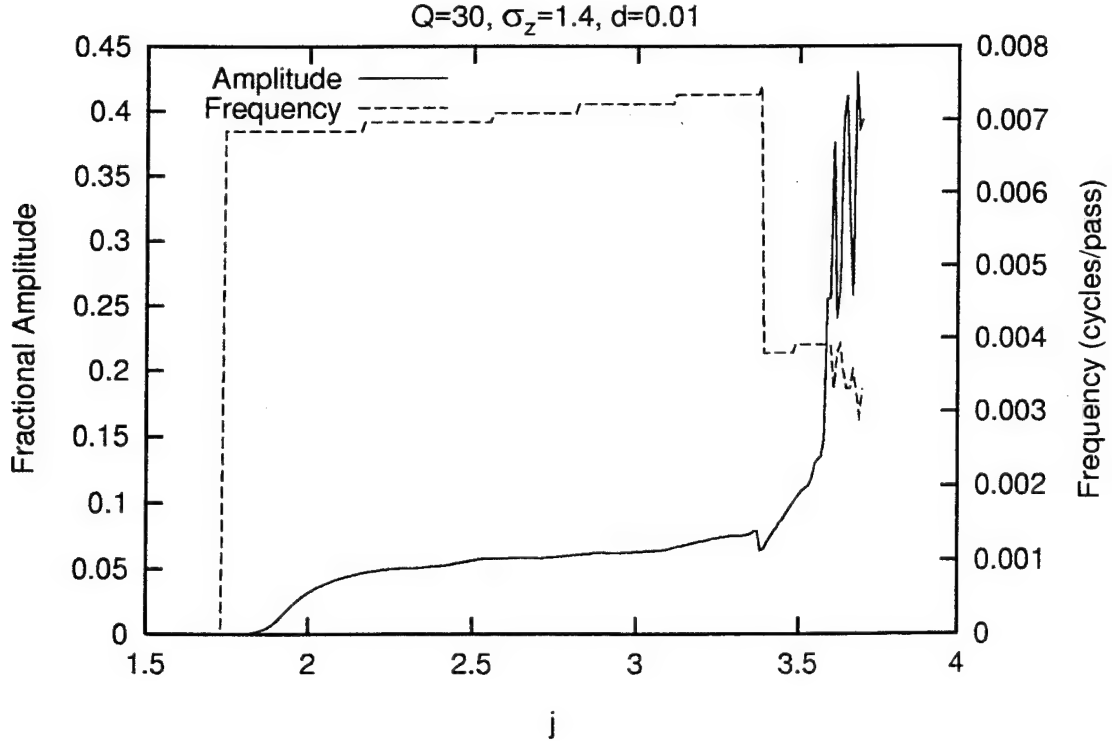


Figure 12. Limit-Cycle Amplitude and Frequency vs.  $j$  for  $Q=30$ ,  $\sigma_z = 1.4$ , and  $d = 0.01$ .

$|a(z, n)|$ . The optical subpulses reach maximum at different values of  $z$ , but decay at approximately the same point as they reach the front of the optical pulse. The higher optical fields raise the threshold for this new sideband and it subsequently decays, which can be seen in the middle-center plot of  $P(v, n)$ . The changes in the optical field amplitude cause corresponding changes in the phase velocity giving maximum gain. This causes the centroid of the power spectrum,  $P(v, n)$  to no longer oscillate smoothly but shift as the number of subpulses in the optical pulse changes. These larger variations of the optical field amplitude result in larger oscillations of the power. The oscillations of  $P(n)$  are no longer sinusoidal in nature, but are somewhat more intricate indicating additional frequencies present. The size of the subpulses and the number of subpulses within the optical pulse continuously changes cause large oscillations of the optical power. The frequency of these oscillations is less than that

for the stable limit-cycle and could be indicative of a period-doubling bifurcation [20].

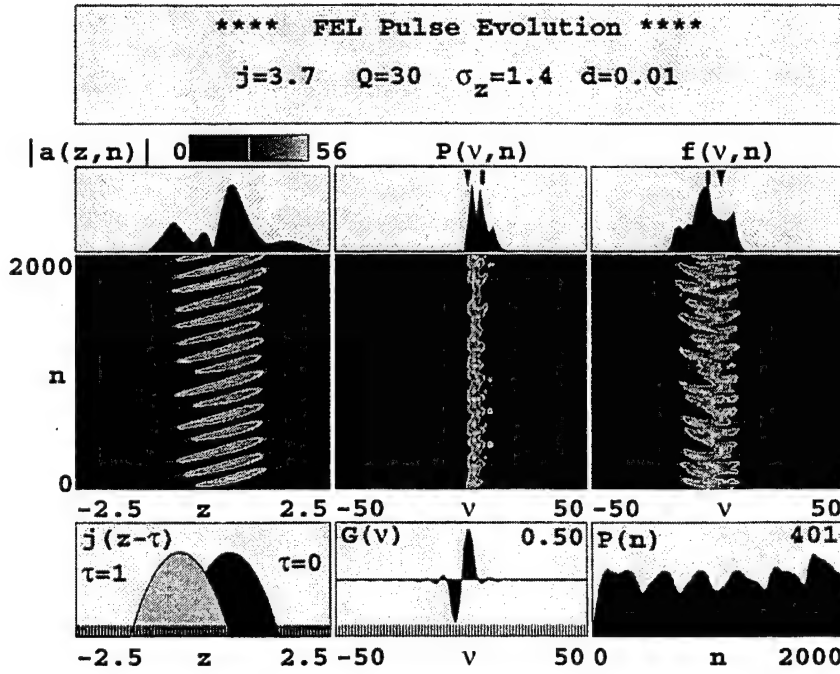


Figure 13. Pulse evolution simulation for  $j = 3.70$ ,  $Q = 30$ ,  $\sigma_z = 1.4$ , and  $d = 0.01$

At different combinations of  $j$ ,  $Q$ ,  $\sigma_z$ , and  $d$ , the variations in the stable limit-cycle oscillations are similar. Figure 14 is the frequency and amplitude of the limit-cycle oscillations for various values of  $j$  with  $Q = 10$ ,  $\sigma_z = 1.4$ , and  $d = 0.01$ . The shape of the curve in the stable limit-cycle region is similar to that for the high  $Q$  resonator, however, the field amplitudes within the optical pulse are much greater than those required for synchrotron oscillations. For this value of  $Q$ , the pulse is modulated by the synchrotron oscillations at  $j \geq 6$ , lower than that required to start the limit-cycle oscillations,  $j \geq 8.5$ . For low  $Q$ , the optical pulse shape is narrow and sharply peaked due to large losses in the forward part of the pulse. Even though the optical pulse is modulated by the synchrotron frequency, the modulation frequency remains below threshold due to the low  $Q$  and the subpulse never completely forms. Thus, the

subpulse remains small relative to the main pulse. The passage of the smaller subpulse through the main pulse has little effect on the power since the total area encompassed by the optical field envelope changes very little during the process.

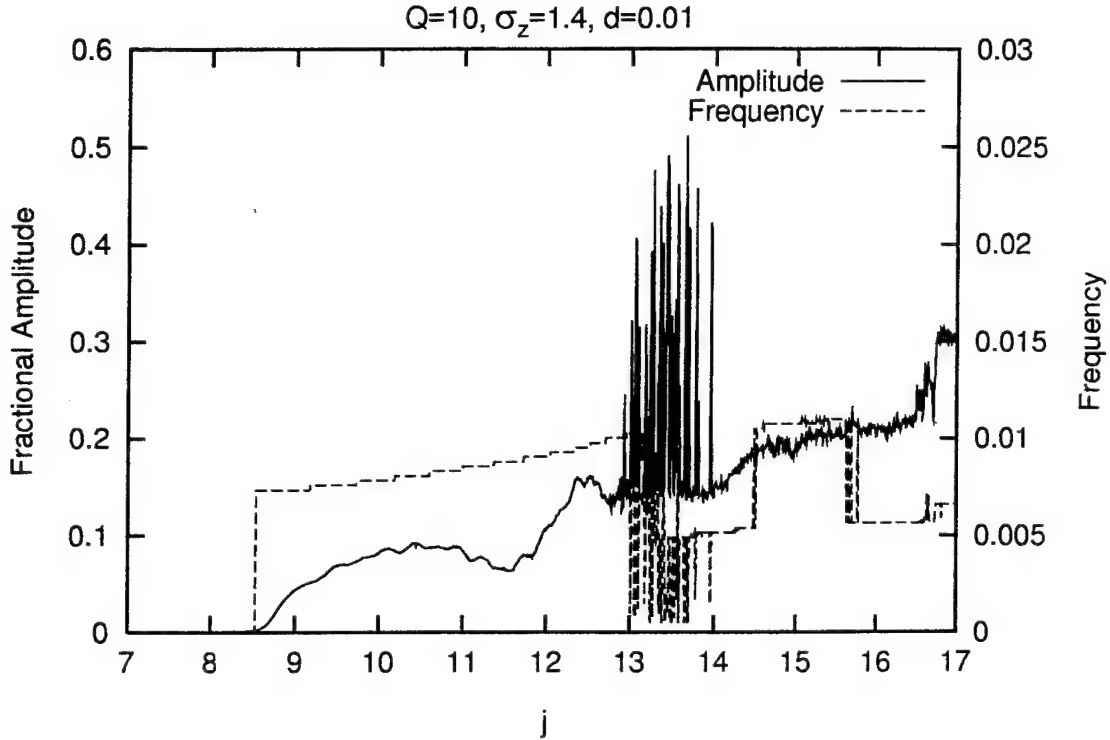


Figure 14. Limit-Cycle amplitude and frequency vs  $j$  for  $Q = 10$ ,  $\sigma_z = 1.4$ , and  $d = 0.01$ .

Figure 15 shows the pulse evolution for  $j = 8$ ,  $Q = 10$ ,  $\sigma_z = 1.4$ , and  $d = 0.01$ . The optical field amplitudes in the forward part of the optical pulse are well above those required to cause synchrotron oscillations,  $|a(z, n)| = 46 \geq 4\pi^2$ , and the optical pulse can be seen to be partially modulated in the upper-left plot of  $|a(z, n)|$ . A small sideband can be seen in the upper-middle plot of  $P(v, n)$  at the synchrotron frequency. However, the sideband is small relative to the carrier and once steady-state is achieved no limit cycle behavior occurs. The oscillations do not begin unless the current density is large enough to raise the modulation frequency above threshold and give a gain per pass that results in appreciable growth of the subpulse as it



moves forward. A similar effect occurs for small values of desynchronism. This again implies the bifurcation resulting in the limit-cycle is a complicated function of  $j$ ,  $Q$ ,  $\sigma_z$ , and  $d$ .

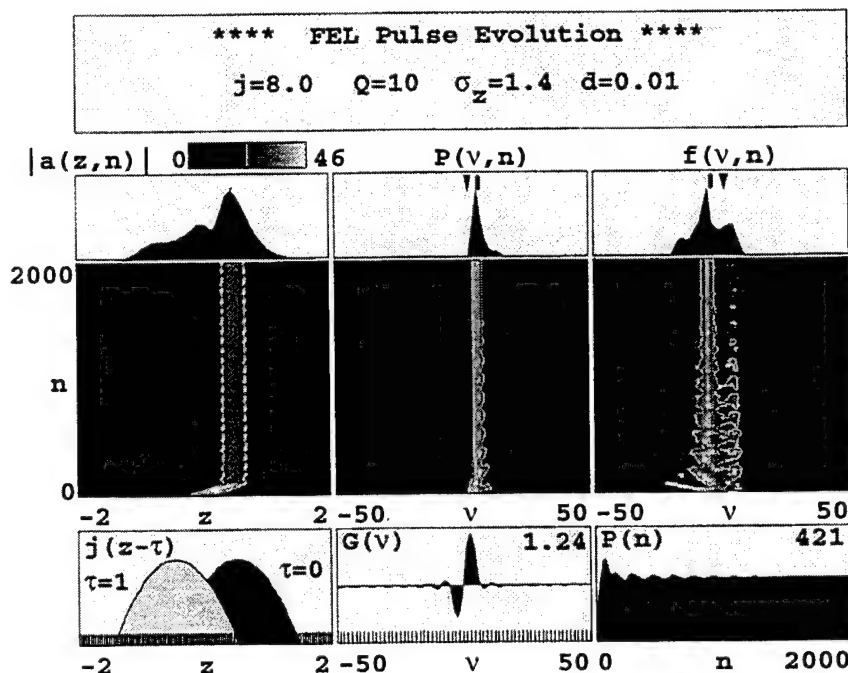


Figure 15. Pulse evolution simulation for  $j = 8.0$ ,  $Q = 10$ ,  $\sigma_z = 1.4$ , and  $d = 0.01$ .

At  $j \geq 13$ , the operation passes through a second bifurcation and enters an unstable region. The limit-cycle transitions to solutions characterized by periods of stable limit-cycle behavior interspersed with chaotic bursts and solutions which appear completely chaotic. A similar effect was observed for the higher  $Q$  solution shown in Figure 12. The amplitude of the power oscillations in this region is very dependent on the input parameters and can change by a large fraction for a small change in  $j$  and is indicative of a chaotic solution. A "crisis" is defined as sudden changes in the chaotic dynamics of a dissipative system as a control parameter is varied [20]. In a boundary or exterior crisis, a dissipative system can move from a chaotic solution to a bounded,

periodic solution [20]. At  $j \geq 14.5$ , the solution passes through what may be a boundary crisis and returns to a stable periodic solution, which can be seen in Figure 14. Figure 16 is a spectral analysis of the power oscillations in the stable limit-cycle region,  $j = 11$ , and the unstable region  $j = 13.5$ , and  $j = 17$ . The plots on the left are  $P(n)$  and the plots on the right are the spectral density of the limit-cycle oscillations. The change in the spectral density between  $j = 11$  and  $j = 13.5$  is typically observed for dissipative systems in a transition from a fixed point to a chaotic solution via the Hopf bifurcation and period doubling cascade [19]. However, the periodic behavior of the oscillation returns for  $j \geq 14.5$  as can be seen in the lower plots of Figure 16. Similar behavior is observed for  $Q$ ,  $\sigma_z$ , and  $d$ .

Hahn and Lee have suggested that the period of the limit cycle is related to the period of the synchrotron oscillations [19]. This has been confirmed experimentally with the FELIX laser [23]. In Figures 12 and 14, in the stable limit-cycle region,  $j \approx 1.8 \rightarrow 3.4$  and  $j \approx 8.5 \rightarrow 12$  respectively, the frequency of the limit-cycle rises and may indicate a dependence on the synchrotron frequency.

## 2. Resonator Quality Factor $Q$

The resonator quality factor  $Q$  is the number of passes through the resonator required for the optical power to decay by  $1/e$  in the absence of gain. In the dissipative dynamics of the FEL oscillator,  $Q$  provides damping which affects the system response and the shape of the optical pulse. Low values of  $Q$ , high loss per pass, tend to shorten the response time of the oscillator and shorten the optical pulse. High values of  $Q$ , low loss per pass, lengthens the response time and lengthens the optical pulse. Low values of  $Q$  also require a higher gain per pass to allow a given mode to reach threshold and saturate. It is not surprising then, that the location of the bifurcation points is dependent upon  $Q$ .

Figure 17 shows the variation of the limit-cycle amplitude as  $Q$  is varied for  $j = 2.5$ ,  $\sigma_z = 1.4$ , and  $d = 0.01$ . The start of the limit-cycle for a given  $j$ ,  $\sigma_z$ , and  $d$

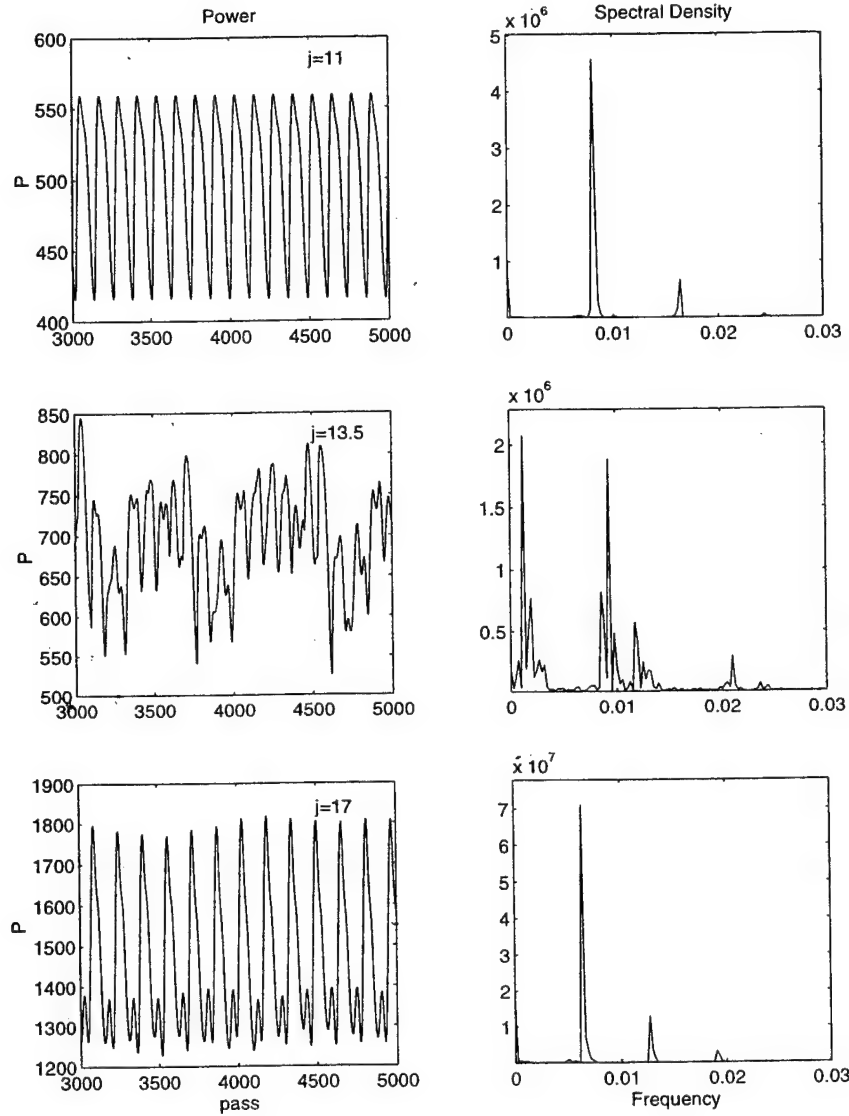


Figure 16. Power and power spectral density at various values of  $j$ , for  $Q = 10$ ,  $\sigma_z = 1.4$ , and  $d = 0.01$ .

begins when  $Q$  is large enough to allow the synchrotron frequency,  $\nu_s = \sqrt{|a|}$ , to reach threshold and saturate. Similar to the behavior with  $j$ , once this mode reaches saturation, the optical pulse becomes modulated and the subpulses form. As with  $j$ , the trapped-particle instability is a necessary, but not a sufficient condition for the limit-cycle to occur. The synchrotron oscillations must be present and the mode must

be above threshold for the subpulses to form and grow to a significant fraction of the main pulse. The limit-cycle does not commence until  $Q \geq 20$ . Once the bifurcation point is passed the system enters a stable limit-cycle region. The amplitude of the limit-cycle increases slightly over the range of  $Q \approx 20 \rightarrow 55$ , and the frequency of the limit-cycle increases slightly. The shape of the curve in this region is qualitatively similar to that for the stable limit-cycle region plotted against  $j$ . For  $Q \geq 55$  the system passes through a second bifurcation. As with the second bifurcation for  $j$  the frequency of the limit-cycle decreases and the amplitude of the oscillations increase. Once the unstable region is reached,  $Q \geq 60$ , the output is extremely dependent on the initial conditions, indicating as  $Q$  is increased past this point and the system tends toward chaotic behavior.

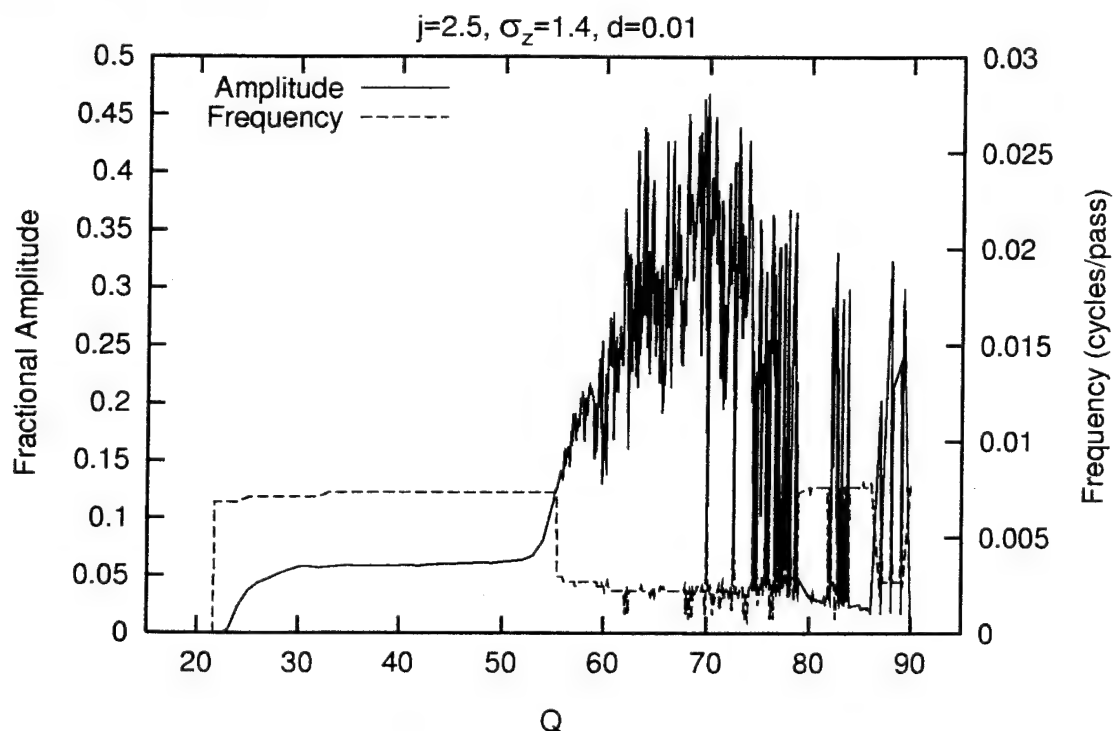


Figure 17. Limit-cycle Amplitude vs  $Q$  for  $j = 2.5$ ,  $\sigma_z = 1.4$ ,  $d = 0.01$ .

Figure 18 follows the pulse evolution for  $j = 2.5$ ,  $Q = 60$ ,  $\sigma_z = 1.4$ , and  $d = 0.01$ . The optical pulse in this region is relatively wide, typically  $5 \rightarrow 10$  slippage distances.

Within the main pulse are many subpulses with the majority of the optical power in the two rear subpulses. Small subpulses form in the forward part of the pulse due to the slower response time of the oscillator resulting from the higher  $Q$ . As with  $j$ , local field amplitudes within the subpulses can vary for a given pass which move the synchrotron modulation above and below threshold. This causes the subpulses to reach their maximum closer or farther from the centroid for a given pass, and changes the number of large subpulses within the main pulse at a given time. The large number of subpulses can be seen in the upper-left plot of  $|a(z, n)|$  on the final pass. The spatial change over time in subpulse formation can be seen in the middle-left plot of  $|a(z, n)|$ . Again as with  $j$ , the varying optical field amplitude causes sidebands to grow and decay as its frequency moves above and below threshold. The temporal change in the spatial modulation results two large subpulses alternating with only one large subpulse. The result is a large amplitude power oscillation and a lower frequency of the limit cycle.

As  $Q$  is increased further, the power oscillations continue to be large relative to the average power, and are characterized by intricate patterns indicating additional frequencies present and may indicate a period-doubling cascade [20]. Figure 19 follows the spectral density change of the limit-cycle as it moves from the stable into the unstable region and beyond. The spectral density of the power oscillations grows from being dominated by a single frequency as seen in the upper plot of power and power spectral density for  $Q = 54$  to being composed of a number of frequencies seen in the middle two plots of  $Q = 60$  and  $Q = 70$  respectively. This again is typical of a period-doubling cascade [20]. At  $Q \geq 75$  the system may pass through a boundary crisis. The solution moves back towards a stable limit-cycle with small amplitude oscillations. This is shown in the lower plot of the spectral power density for  $Q = 85$ . Figure 20 follows the pulse evolution for  $j = 2.5$ ,  $Q = 85$ ,  $\sigma_z = 1.4$  and  $d = 0.01$ . In this region a dynamic is established in which the growth of the subpulses moving forward from the rear of the main pulse matches the decay of the subpulses moving

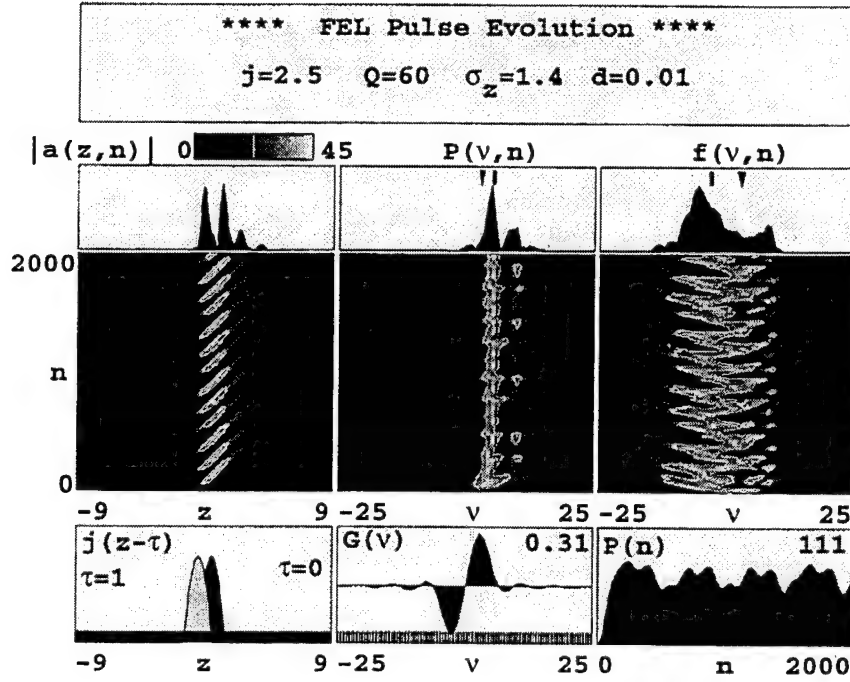


Figure 18. Pulse evolution simulation for  $j = 2.5$ ,  $Q = 60$ ,  $\sigma_z = 1.4$ , and  $d = 0.01$ .

into the forward part of the main pulse. The modulation of the main pulse is relatively constant over time and results in small area change of the optical pulse. This results in small oscillations of the power relative to the average power. The stable modulation results in a sideband at  $v + v_s$  that is as large as the carrier and in a smaller sideband at  $v + 2v_s$  which can be seen in the upper-middle plot of  $P(v, n)$ . The carrier and the sidebands are temporally stable indicating the optical field amplitude is relatively stable in time. The result is relatively stable power which can be seen in the lower-right plot of  $P(n)$ . Different values of  $j$ ,  $\sigma_s$ , and  $d$  affect the value of  $Q$  where the synchrotron modulation is raised above threshold, and thus the value of  $Q$  where the limit-cycle begins. Higher values of  $j$  and  $\sigma_z$  tend to raise the gain per pass and lower the threshold for the trapped-particle instability. For these cases, the limit-cycle starts at lower values of  $Q$ . Higher values of  $d$  can either raise or lower the value of  $Q$  at

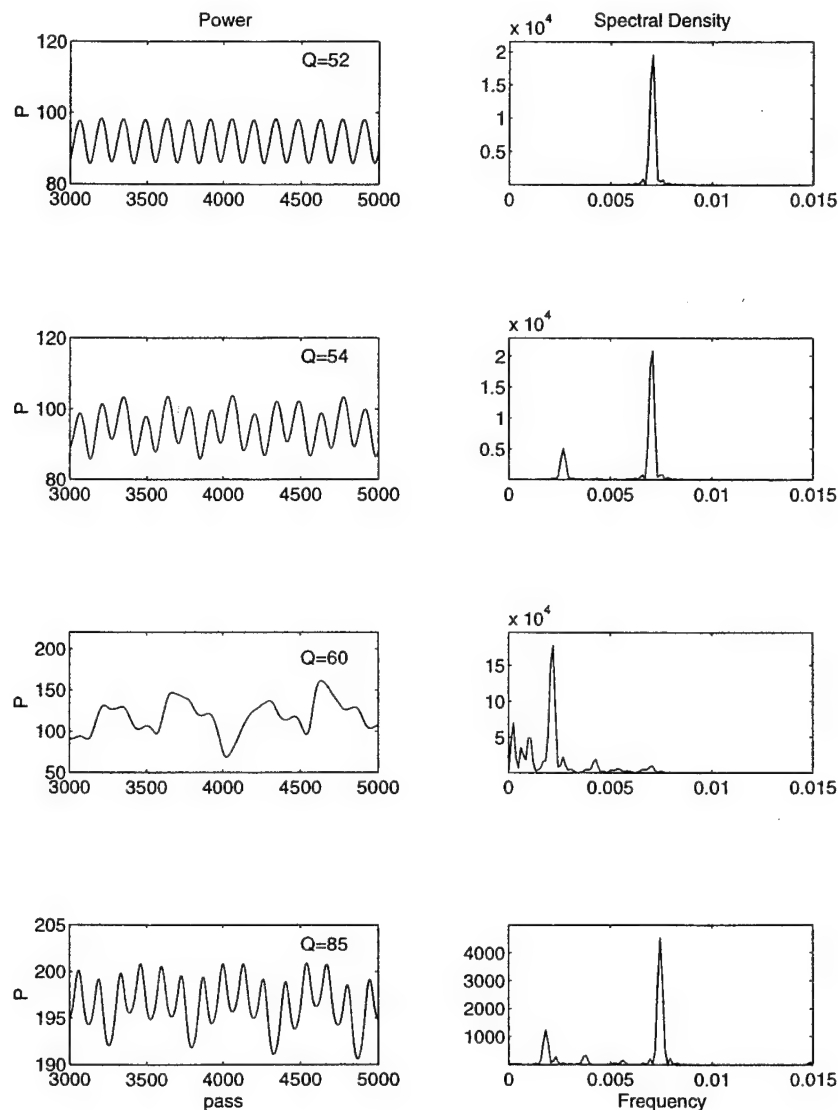


Figure 19. Power and Power Spectral Density at various values of  $Q$  for  $j = 2.5$ ,  $\sigma_z = 1.4$ , and  $d = 0.01$ .

which the limit cycle starts, since the slope of gain versus desynchronism changes over the range of  $d$ .

Figure 21 shows the variation of the amplitude of the limit-cycle versus  $Q$  holding  $j = 2.5$ ,  $\sigma_z = 0.7$ , and  $d = 0.01$ . The shorter pulse length results in overall reduced coupling between the optical and electron pulses and requires a higher  $Q$  to start the

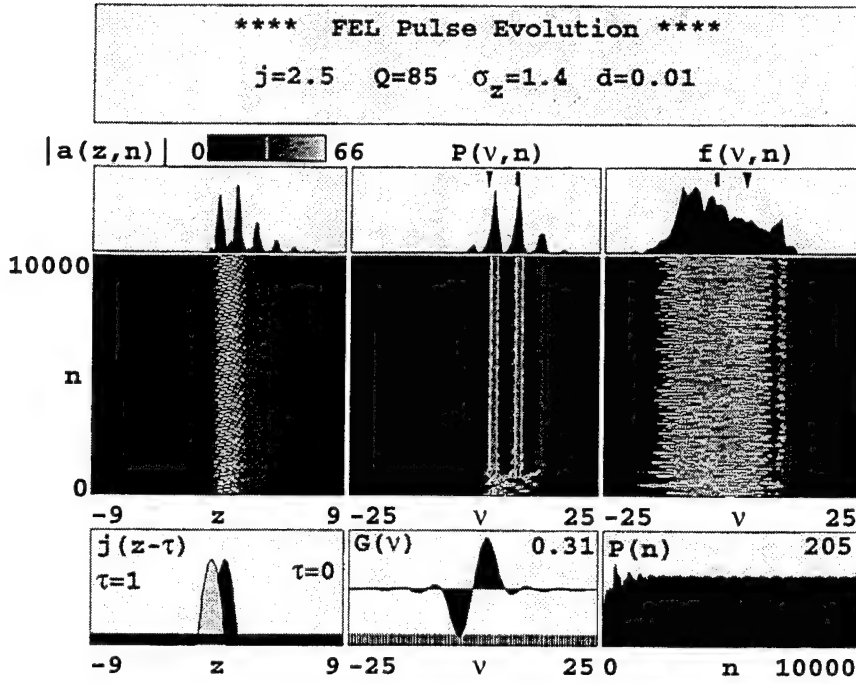


Figure 20. Pulse evolution simulation for  $j = 2.5$ ,  $Q = 85$ ,  $\sigma_z = 1.4$ , and  $d = 0.01$ .

limit-cycle. The amplitude variation of the stable limit-cycle region for  $\sigma_z = 1.4$  is also plotted for reference. At the shorter pulse length of  $\sigma_z = 0.7$ , the optical field amplitudes remain too low to cause much more than one synchrotron oscillation over the entire range of  $Q$ . The limit-cycle remains stable over this entire range and the amplitude of the oscillations relative to the average power decreases.

### 3. Electron Pulse Length $\sigma_z$

The electron pulse length affects the optical pulse gain through the current density. A longer pulse increases the gain over the optical pulse, since the optical pulse experiences a higher average current density over the interaction distance,  $N\lambda$  [16] [22]. A longer electron pulse length results in a higher optical amplitude at steady-state for a given  $j$ ,  $Q$ , and  $d$ . The onset of the trapped-particle instability will



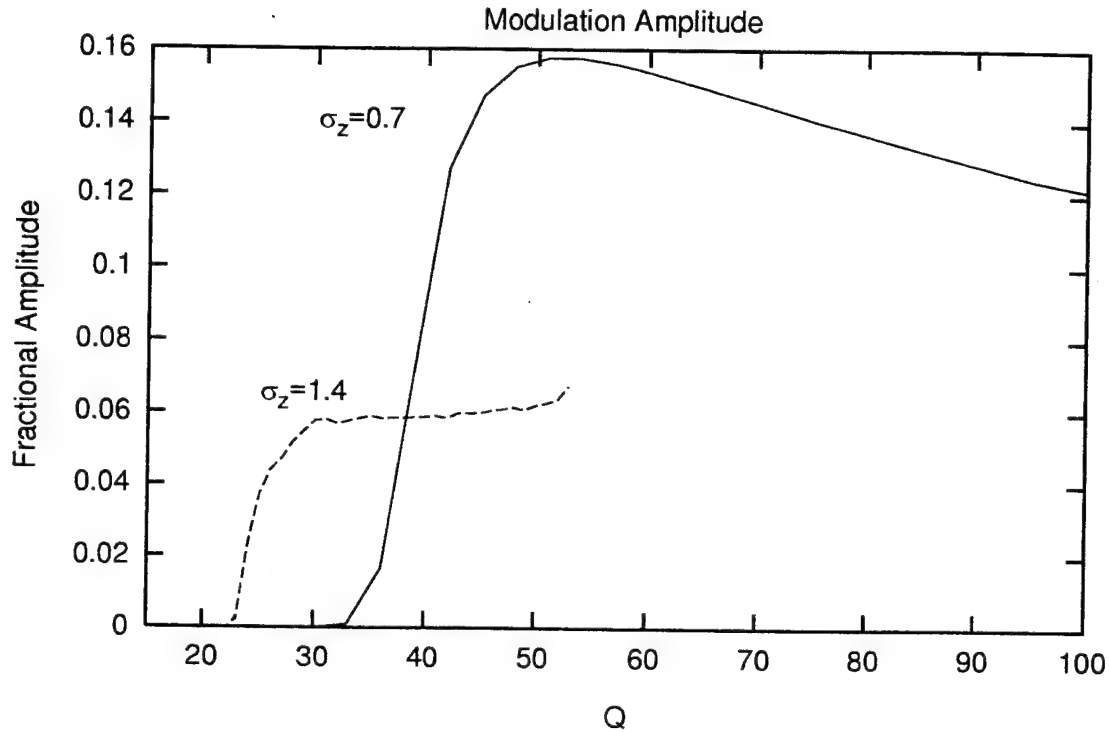


Figure 21. Limit-cycle amplitude vs  $Q$  for  $j = 2.5$ ,  $\sigma_z = 0.7$ ,  $d = 0.01$ . Limit-cycle vs  $Q$  for  $\sigma_z = 1.4$  is plotted for reference (dashed-line).

occur when  $\sigma_z$  is large enough to result in optical field amplitudes large enough to raise the synchrotron modulation above threshold. At low  $j \approx 1$ , the limit-cycle begins when the optical field amplitude is great enough to cause approximately one-half synchrotron oscillation [15] [18]. Figure 22 shows the amplitude and frequency of the limit-cycle dependence on  $\sigma_z$  holding  $j = 2.5$ ,  $Q = 30$ ,  $d = 0.01$ . Again, the amplitude of the limit-cycle is plotted relative to its average power. In general, as  $\sigma_z$  is varied, no limit-cycle is observed until strong optical fields result in the trapped-particle instability.

For the values of  $j$ ,  $Q$ , and  $d$  used in Figure 22, the limit-cycle begins when  $\sigma_z \geq 1.0$ . The size of the oscillations grows until  $\sigma_z \approx 1.2$  and decreases until  $\sigma_z \approx 1.7$ . At this  $\sigma_z$  the optical field amplitudes are large enough for approximately one full synchrotron oscillation in a slippage distance,  $N\lambda$ . The relative size of the

oscillations then increases slightly until  $\sigma_z \approx 2.2$  where the oscillator reaches a second bifurcation. The frequency of the oscillations remain constant through this range. At  $\sigma_z \geq 2.2$  the limit-cycle enters a region where the amplitude of cycle increases dramatically and its primary frequency decreases by approximately a factor of five.

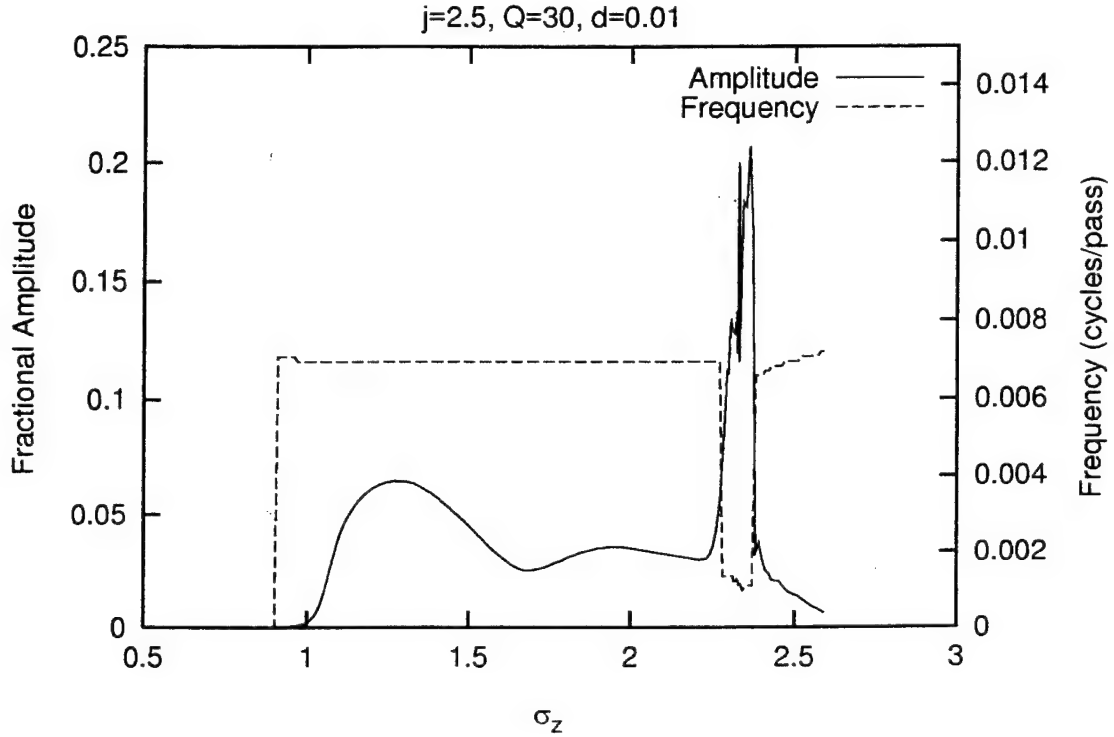


Figure 22. Limit-cycle amplitude and frequency vs  $\sigma_z$  for  $j = 2.5$ ,  $Q = 30$ , and  $d = 0.01$ .

Figure 23 follows the pulse evolution for  $j = 2.5$ ,  $Q = 30$ ,  $\sigma_z = 2.32$  and  $d = 0.01$ . This point corresponds to the pulse length near the amplitude oscillations in Figure 22. There are now two processes occurring within the optical pulse. The subpulses moving forward account for the higher frequency "ripples" in the power seen in  $P(n)$  in the lower-right plot of Figure 23. Again, as with  $j$  and  $Q$ , there is a temporal change in the modulation of the optical pulse which results in passes where the optical pulse is composed of one large subpulse and two relatively small subpulses alternating with passes where the optical pulse is composed of two large

subpulses. The higher optical fields resulting from two large subpulses lowers the gain per pass and the modulation sideband falls below threshold. This combination of the control parameters cannot maintain a spatial modulation of two large subpulses. The energy distribution of the electrons, the middle-right plot,  $f(v, n)$  follows the change in the optical field amplitude. The spread in the distribution is a roughly a measure of the peak-to-peak height of the separatrix [1]. The distribution spreads at the power peak and stronger optical fields occurring when the two large subpulses comprise the optical pulse. The variation in the strength of the modulation of the optical pulse is also shown in the middle-center plot of optical spectrum,  $P(v, n)$ . A sideband grows and decays as the threshold is raised and lowered. The alternation of the optical pulse between a single large subpulse with two minor subpulses and two large subpulses requires more passes than the subpulses moving forward and accounts for the lower frequency, "sawtooth" form of power oscillations seen in the lower-right plot of  $P(n)$ .

The output of the oscillator is very dependent on the initial conditions in this region. The size of the oscillations can change by a large amount by as little a change as  $\Delta\sigma_z \approx 0.001$ . Figure 24 is a spectral analysis of the power oscillations at various points across the large amplitude region. The spectral analysis shows the growth of a lower frequency component starting at  $\sigma_z \geq 2.25$  which can be seen in the left-center plot of the power and in the right-center plot of power spectral density for  $\sigma_z = 2.27$ . The lower frequency oscillation is completely established by  $\sigma_z \approx 2.3$  as seen in the lower plots of power and the power spectral density in Figure 24. At  $\sigma_z \geq 2.4$ , the system returns to stable limit-cycle oscillation with small amplitude as shown in Figure 22. This size pulse length can sustain two large subpulses and the modulation frequency returns to approximately that of the subpulses moving forward.

Different combinations of  $j$ ,  $Q$ , and  $d$ , change the  $\sigma_z$  needed to start the limit-cycle. However, the overall features of the stable limit cycle remain the same. Figure 25 shows the dependence of the relative amplitude of the limit-cycle on  $\sigma_z$  in the

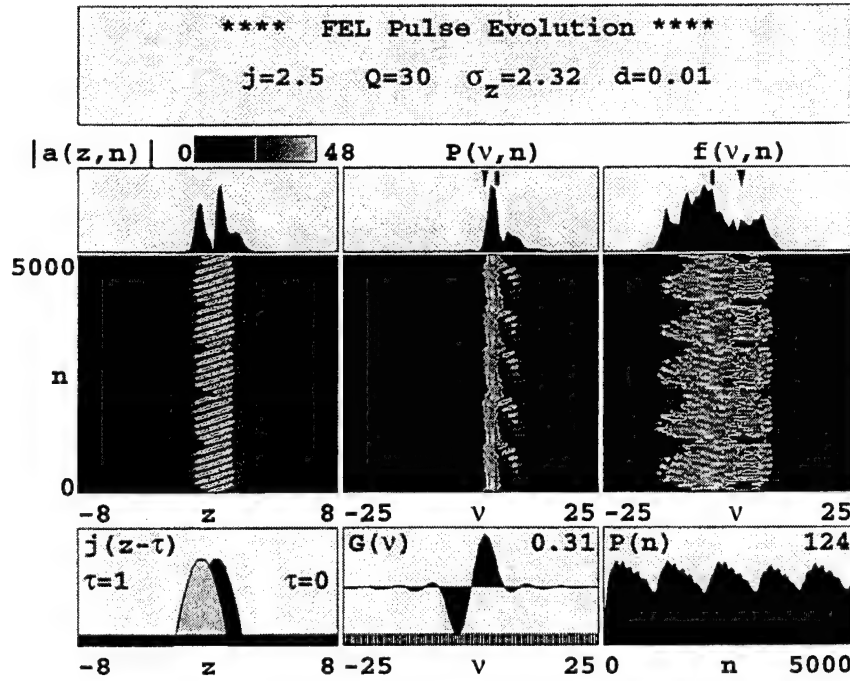


Figure 23. Pulse evolution simulation for  $j = 2.5$ ,  $Q = 30$ ,  $\sigma_z = 2.32$ , and  $d = 0.01$ .

stable region for  $j = 10$ ,  $Q = 10$ , and  $d = 0.01$ . Also plotted is the relative amplitude for  $j = 2.5$ ,  $Q = 30$ , and  $d = 0.01$  for reference. The higher  $j$  and lower  $Q$  start the limit-cycle at a longer pulse length than the lower  $j$  and higher  $Q$ . The optical field amplitudes reach levels well above those required for the synchrotron oscillations,  $|a| \geq 4\pi^2$ , prior to the start of the limit-cycle for the higher  $j$  and lower  $Q$ . Again this shows the trapped-particle instability is a necessary but not sufficient condition for the limit-cycle to begin. Other values of  $j$  and  $Q$  result in qualitatively the same behavior in the stable region. Also, once  $\sigma_z$  is increased above a certain value, again dependent on the other parameters, the system enters an unstable region of operation.

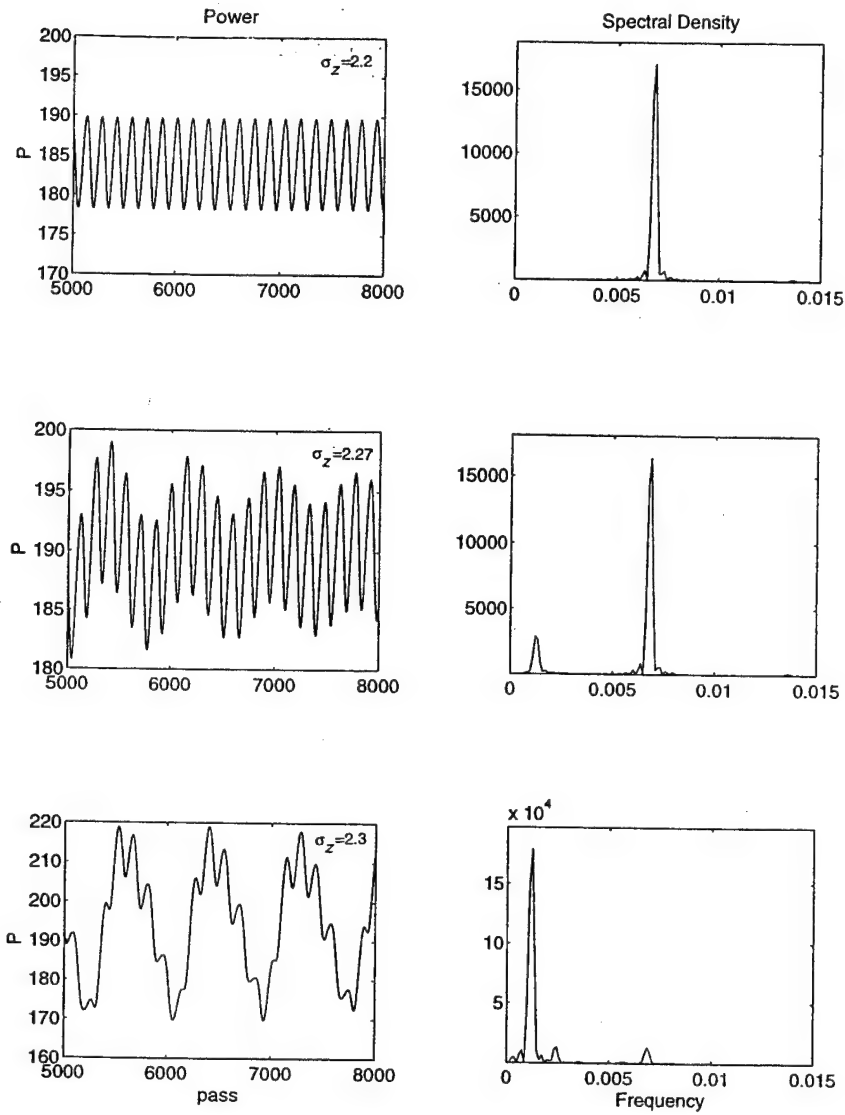


Figure 24. Power and Power Spectral Density for  $\sigma_z = 2.2, 2.27$ , and  $2.3$ , with  $j = 2.5$ ,  $Q = 30$ , and  $d = 0.01$ .

#### 4. Desynchronism $d$

The current density,  $j$ , and to a lesser extent, the resonator quality factor,  $Q$ , determine the size of the limit-cycle oscillations. The desynchronism mechanism determines the rate at which the subpulses move through the main pulse, and therefore the frequency of the oscillations. The relationship between  $d$  and the period

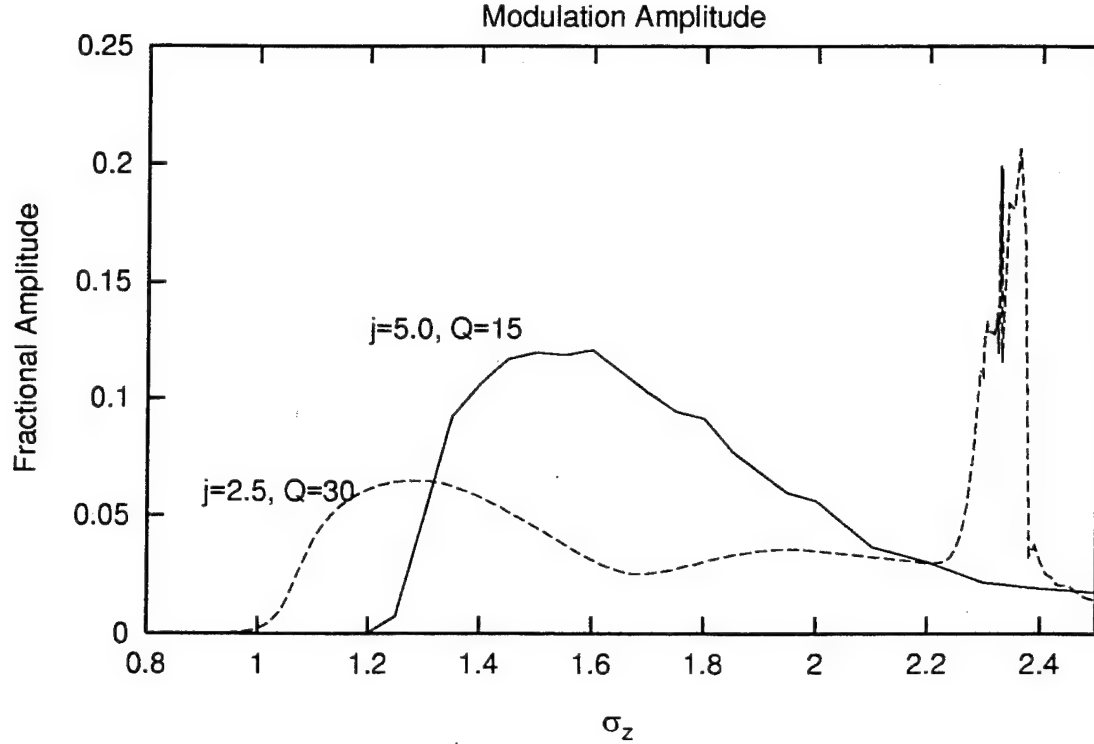


Figure 25. Limit-cycle amplitude vs.  $\sigma_z$  for  $j = 10$ ,  $Q = 10$ , and  $d = 0.01$ . Also plotted is the amplitude vs.  $\sigma_z$  for  $j = 2.5$ ,  $Q = 30$  for reference (dashed-line).

of the limit-cycle was noted when the first limit-cycle was observed [21]. Hahn and Lee later modified the relationship to account for subpulse shortening due to the synchrotron modulation [19]. The desynchronism-gain relationship determines whether the optical pulse moves forward, remains stationary, or falls behind relative to the electron pulse [22]. If the desynchronism is small enough, the limit-cycle behavior does not occur, even though the optical field amplitudes are large enough to cause the trapped-particle instability and the pulse is fully modulated. In this range of desynchronism, the optical pulse is characterized by a narrow and highly peaked main pulse with a small subpulse an order of magnitude smaller. The desynchronism provides little gain in this range to raise the modulation above threshold and cause sideband growth. The relatively small subpulse moving very slowly through the main pulse causes little effect and could explain why no limit-cycle oscillations were

observed with FELIX at small values of desynchronism [23].

Figure 26 shows the dependence of the amplitude of the limit-cycle on  $d$  for  $j = 2.5$ ,  $Q = 30$ , and  $\sigma_z = 1.4$ . Also plotted is the optical power. The start of the limit-cycle does not correspond to optical power maximum. This relationship is observed for all combinations of  $j$ ,  $Q$ , and  $\sigma_z$  analyzed. The rise in the optical power when the limit-cycle commences was also observed for different combinations of  $j$ ,  $Q$ , and  $\sigma_z$ . Figure 27 shows the dependence of limit-cycle amplitude on  $d$  holding  $j = 2.5$ ,  $Q = 30$ , and  $\sigma_z = 2.0$ . The power rise when the limit-cycle starts exceeds the peak power rise resulting from the desynchronism.

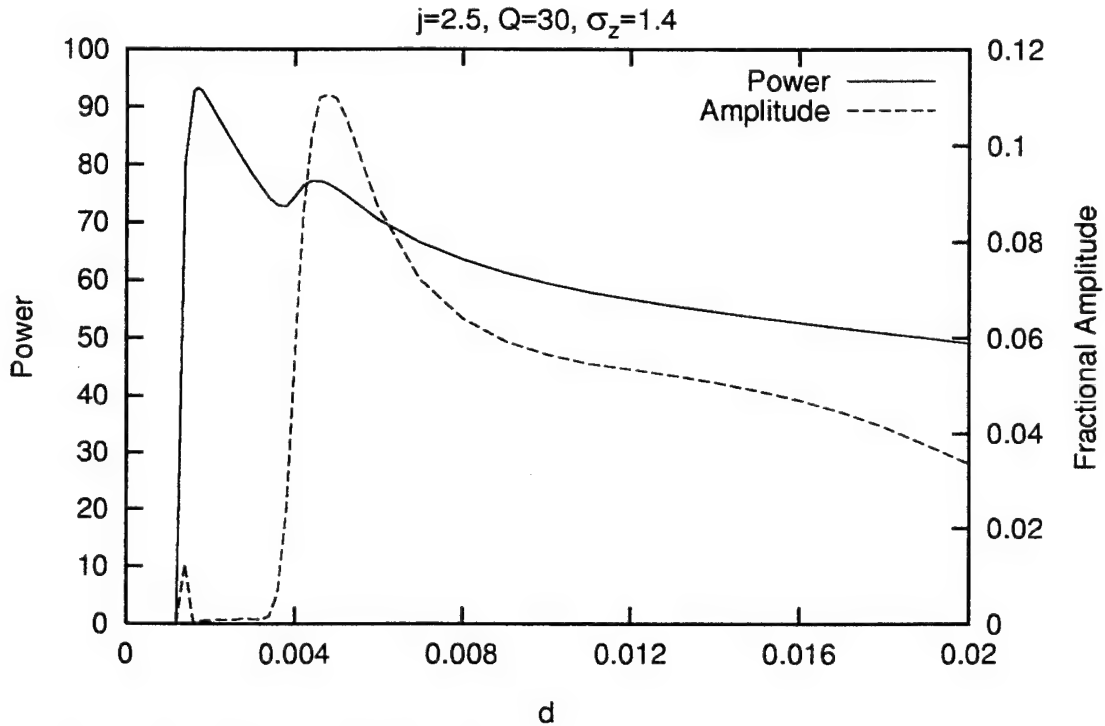


Figure 26. Power and Limit-cycle amplitude vs.  $d$  for  $j = 2.5$ ,  $Q = 30$ ,  $\sigma_z = 1.4$ .

Figure 28 follows the pulse evolution for  $j = 2.5$ ,  $Q = 30$ ,  $\sigma_z = 1.4$  and  $d = 0.0017$  and corresponds to the point on Figure 26 at the maximum power. The optical pulse is very narrow and peaked as can be seen in the upper-left plot of  $|a(z, n)|$  on the final pass. The middle-left plot of  $|a(z, n)|$  shows the pulse

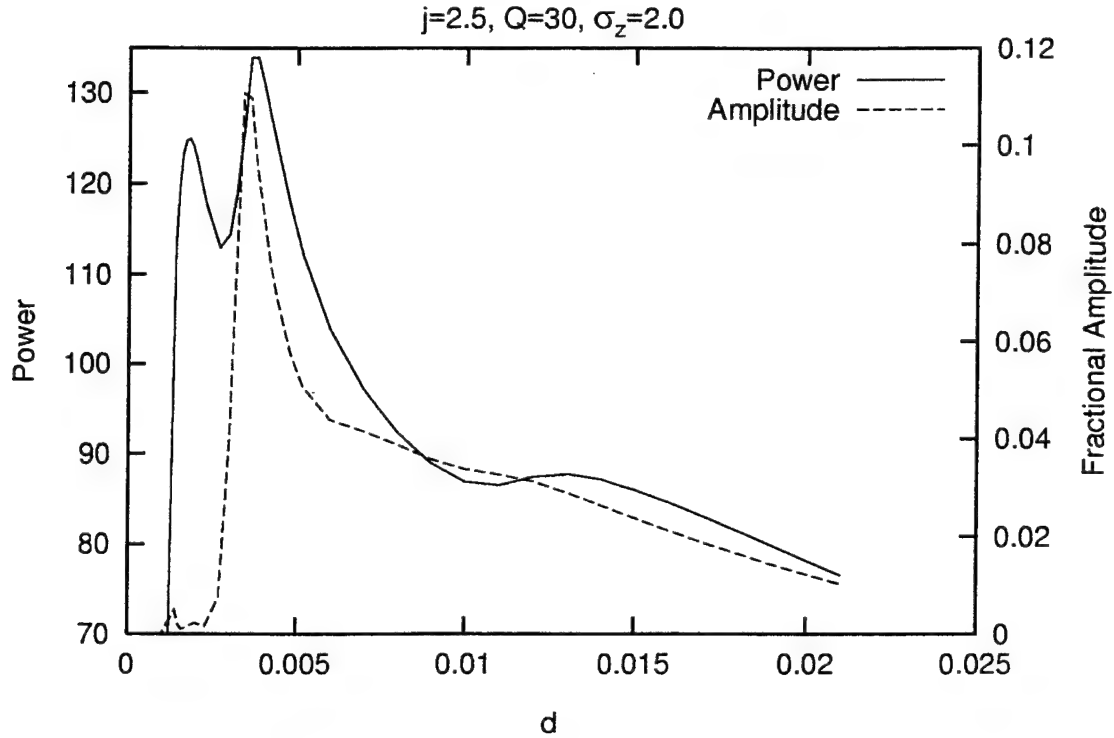


Figure 27. Power and Limit-cycle amplitude vs.  $d$  for  $j = 2.5$ ,  $Q = 30$ ,  $\sigma_z = 2.0$ .

maintains its shape over many passes. The subpulses move forward very slowly, are relatively small, and no limit-cycle behavior occurs.

As  $d$  is increased further, the steady-state power reached decreases. However, the gain resulting from the desynchronism increases towards its maximum [22]. Eventually, the gain increase from the desynchronism raises the synchrotron modulation above threshold and the limit-cycle starts. The amount of desynchronism required to start the limit-cycle behavior is dependent upon the parameters of  $j$ ,  $Q$ , and  $\sigma_z$ . Figure 29 compares the limit-cycle amplitude dependence on  $d$  for  $\sigma_z = 1.4$  and  $\sigma_z = 2.0$ ; the values of  $\sigma_z$  used in Figures 26 and 27. The longer pulse length, the dashed-line, couples better with the optical pulse and requires a lower gain per pass to raise the synchrotron modulation above threshold. Thus, the limit-cycle starts at a smaller desynchronism than the smaller pulse length, the solid-line. Figure 30 shows the limit-cycle dependence on  $d$  at two combinations of  $j$  and  $Q$ . The higher  $j$



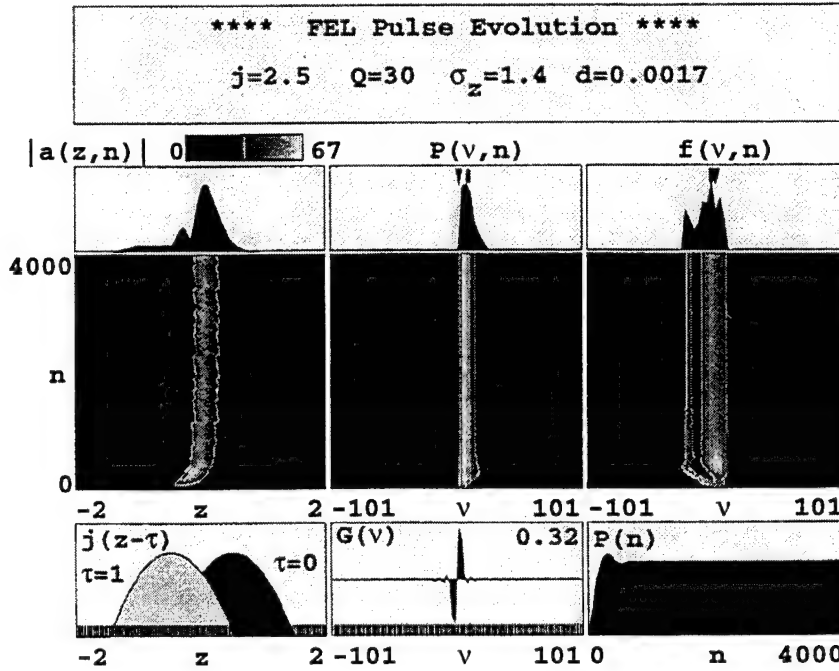


Figure 28. Pulse evolution simulation for  $j = 2.5$ ,  $Q = 30$ ,  $\sigma_z = 1.4$ , and  $d = 0.0017$ .

and lower  $Q$  combination, the dashed-line, requires a higher gain per pass to start the limit-cycle, resulting in the start of the limit-cycle at a larger desynchronism. Again, the bifurcation dependence upon the four physical parameters is clearly shown. In general, for a given  $j$ ,  $Q$ , and  $\sigma_z$ , as  $d$  is increased past the value resulting in the largest power oscillations, the amplitude of the limit-cycle decreases, following the decrease of the optical power at higher desynchronism.

Once the limit-cycle commences the frequency of the cycle is linearly dependent on  $d$  [19] [21] [24]. If the optical pulse formed from the interaction is assumed to be roughly on the order of the slippage distance,  $N\lambda$ , then the longitudinal modulation of the optical pulse resulting from the synchrotron oscillations will shorten the optical pulse and form a subpulse at  $\approx N\lambda 2\pi/v_s$ . Once the modulation begins, the desynchronism mechanism moves the subpulses forward by an amount  $\approx N\lambda d$  on

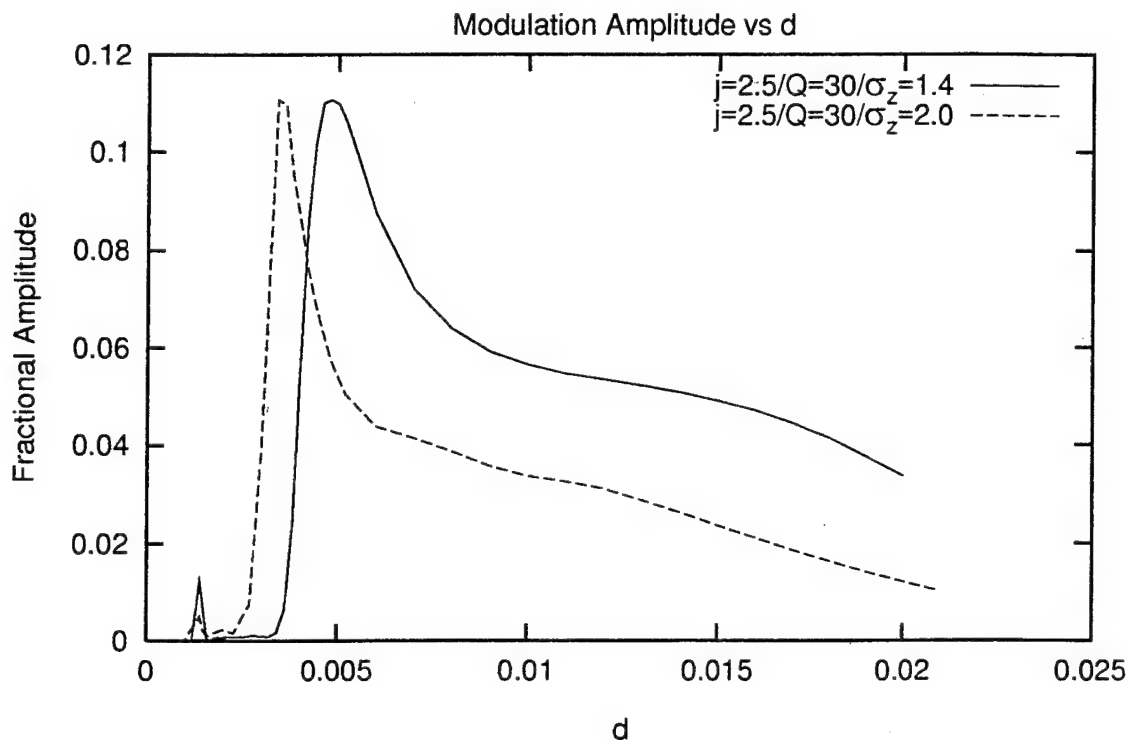


Figure 29. Limit-cycle amplitude dependence on  $d$  for  $j = 2.5$ ,  $Q = 30$ ,  $\sigma_z = 1.4$  and  $\sigma_z = 2.0$ .

each pass. Assuming the newly formed subpulse must replace the forward subpulse prior to the creation of the next subpulse, the frequency of subpulse creation is  $\approx v_s d / 2\pi$ . In the stable limit-cycle region,  $v_s \approx 2\pi$ , so the frequency is  $\approx d$ . Figure 31 shows the linear dependence of the frequency of the limit-cycle on  $d$  for six different combinations of  $j$ ,  $Q$ , and  $\sigma_z$ . However, the slope of the dependence is somewhat less than one and fits  $\approx d/\sqrt{2}$ . It should be noted these frequencies were measured in the stable limit-cycle region only, and the different combinations of the physical control parameters resulted in different optical field amplitudes at the start of the limit-cycle. The desynchronism appears to set the "base" frequency or period of the limit-cycle. Oscillations which resulted in an amplitude less than 0.5% of the power were not plotted in Figure 31 and the points which do not follow the linear dependence occur with amplitudes of less than 1% of the power.

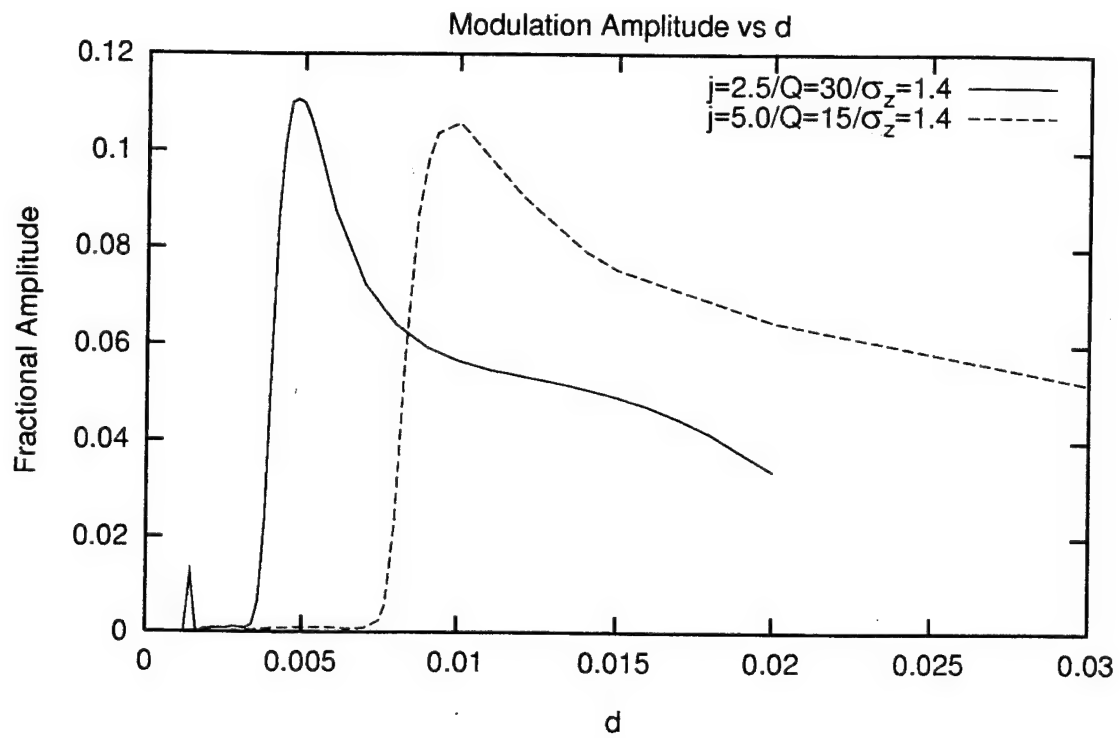


Figure 30. Limit-cycle amplitude dependence on  $d$  for  $j = 2.5$ ,  $Q = 30$ ,  $\sigma_z = 1.4$  and  $j = 5.0$ ,  $Q = 15.0$ ,  $\sigma_z = 1.4$ .

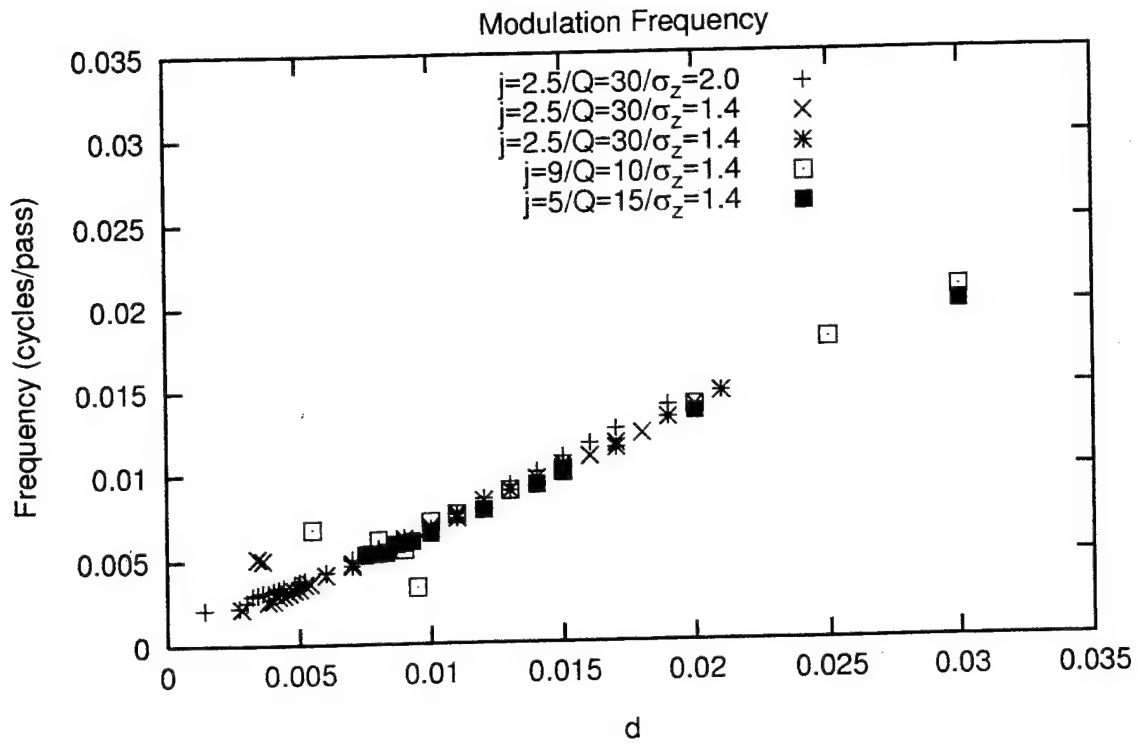


Figure 31. Frequency of the Limit-cycle vs.  $d$  for various combinations of  $j$ ,  $Q$ , and  $\sigma_z$ .

## IV. CONCLUSION

The limit-cycle behavior results from a codimension-four Hopf bifurcation which shifts the operation of the dissipative oscillator from a fixed point solution to a periodic one [19][20]. The four physical input parameters controlling the start of the limit-cycle are the dimensionless current density,  $j$ , the resonator quality factor,  $Q$ , the dimensionless pulse length,  $\sigma_z$ , and the desynchronism,  $d$ . The amplitude of the oscillations is driven by  $j$  and to a lesser extent  $Q$ . The point at which the limit cycle starts for a given parameter is dependent upon the combination of the other three. The frequency of the cycle depends linearly on  $d$ , and weakly on the other three parameters. The trapped-particle instability is a necessary condition for the limit-cycle but is not a sufficient condition. In addition to the trapped-particle instability, the combination of the four parameters must also raise the synchrotron modulation above threshold to permit growth of the subpulses. After the stable limit-cycle, exists an unstable region which results in large power oscillations which are quasiperiodic or chaotic. Following the unstable region is a region where the stable limit cycle returned and may indicate a type of "on-off intermittency " and the existence of boundary crises in the transition to chaos [20].

Areas of addition study include the further investigation of the bifurcation points at many different combinations of the control parameters. From these a "phase-plot" of the limit-cycle could be constructed. This plot would be useful to the FEL designer in avoiding the limit cycle. Also, further investigation of the transition to chaos in the FEL offers a rich source of research.



## LIST OF REFERENCES

1. W. B. Colson, "Classical Free Electron Laser Theory," Chapter 5 in *Laser Handbook*, Vol. 6, W. B. Colson, C. Pellegrini, and A. Renieri (eds.), Elsevier Science Publishing Co. Inc., The Netherlands, 1990.
2. R. Warren, *Star Wars and the FEL*, 1993.
3. C. A. Brau, *Free Electron Lasers*, Academic Press, San Diego, 1990.
4. APS Study: Science and Technology of Directed Energy Weapons, Rev. Mod. Phys., Vol. 59, No.3, Part II, D. Pines, et. al. (eds.), 1987.
5. F. G. Gebhardt, *Applied Optics*, Vol. 15, No. 6, **1479**, 1976.
6. private communication with J. Cook, SPAWAR Code 332.
7. J. D. Jackson, *Classical Electrodynamics*, Wiley, New York, 1976.
8. W. B. Colson, J. Blau, G. Cord, D. Craun, D. Gillingham, D. Kiel, J. H. Park, and R. Souza, "Free Electron Lasers for Inertial Confinement Fusion", Chapter 16, pages 421 to 436, in *Nuclear Fusion by Inertial Confinement*, editors: G. Velarde, Y. Ronen, and J. M. Martinez-Val, CRC Press, Florida, 1992.
9. W. B. Colson, S. K. Ride, *Physics of Quantum Electronics*, Vol. 7, p. 377, 1980.
10. W. H. Louisell, J. F. Lam, D. A. Copeland, W. B. Colson, *Physical Review A*, Vol. 19, No. 1, **288**, 1979.
11. W. B. Colson, A. M. Sessler, "Free Electron Lasers", *Ann. Rev. Nucl. Part. Sci.*, No. 35 **25**, 1985.
12. P. Elleaume, "Free Electron Laser Undulators, Electron Trajectories and Spontaneous Emission", Chapter 4 in *Laser Handbook*, Vol. 6, W. B. Colson, C. Pellegrini, and A. Renieri (eds.), Elsevier Science Publishing Co. Inc., The Netherlands, 1990.
13. M. V. Klein, T. E. Furtak, *Optics*, Wiley, New York, 1986.

14. W. B. Colson, "Chaotic Optical Modes in Free-Electron Lasers", *Proceedings*, SPIE Vol. 453, p.290, 1984.
15. W. B. Colson, R. A. Freedman, *Optics Communications*, Vol. 46, No. 1, **37**, 1983.
16. W. B. Colson, A. Renieri, *J. de Physique*, **44**, C1-11, 1983.
17. G. A. Cord, *Free Electron Laser Short Pulse Simulation and Two-Mode Sideband Analysis*, Master's Thesis, Naval Postgraduate School, 1991.
18. W. B. Colson, *Physics of Quantum Electronics*, **8**, 457, Addison-Wesley, 1982.
19. S. J. Hahn, J. K. Lee, *Physics Letters A*, **176**, 339, 1993.
20. A. H. Nayfeh, B. Balachandran, *Applied Nonlinear Dynamics*, Wiley and Sons, Inc, New York, 1995.
21. D. A. Jaroszynski, R. J. Baker, A. F. G. van der Meer, D. Oepts, and P. W. van Amersfoort, *Physical Review Letters*, **70**, 3142, 1993.
22. K. A. Sturgess, *A Study of the Amplification of Laser and VLF Waves Using a Simple Pendulum Model*, PhD. Dissertation, Naval Postgraduate School, 1993.
23. G.M. Knippels, A. F. G. van der Meer, R. F. X. A. M. Mols, D. Oepts, P. W. van Amersfoort, *Formation of multiple subpulses in a free-electron laser operating in the limit-cycle mode*, submitted Physical Review E, 1995.
24. S. J. Hahn, J. K. Lee, *Physical Review E*, **48**, 2162, 1993.



## INITIAL DISTRIBUTION LIST

- |    |   |   |
|----|---|---|
| 1. | Defense Technical Information Center    | 2 |
|    | 8725 John J. Kingman Rd., STE 0994      |   |
|    | Fort Belvoir, VA 22060-6218             |   |
| 2. | Library, Code 13                        | 2 |
|    | Naval Postgraduate School               |   |
|    | Monterey, California 93943-5002         |   |
| 3. | Professor William B. Colson, Code PH/Cw | 9 |
|    | Department of Physics                   |   |
|    | Naval Postgraduate School               |   |
|    | Monterey, California 93943-5000         |   |
| 4. | Professor Robert Armstead, Code PH/Ar   | 1 |
|    | Department of Physics                   |   |
|    | Naval Postgraduate School               |   |
|    | Monterey, California 93943-5000         |   |
| 5. | Professor K. E. Woehler, Code PH/Wh     | 1 |
|    | Chairman, Department of Physics         |   |
|    | Naval Postgraduate School               |   |
|    | Monterey, California 93943-5000         |   |
| 6. | Doctor George Neil                      | 1 |
|    | CEBAF                                   |   |
|    | 12000 Jefferson Ave.                    |   |
|    | Newport News, Virginia 23606            |   |
| 7. | Doctor Fred Dylla                       | 1 |
|    | CEBAF                                   |   |
|    | 12000 Jefferson Ave.                    |   |

Newport News, Virginia 22245-5200

- |     |   |   |
|-----|---|---|
| 8.  | John Albertine<br>Code 332, Division Director<br>Directed Energy Division<br>Space and Naval Warfare Systems Command<br>2451 Crystal Dr.<br>Arlington, Virginia 23606 | 1 |
| 9.  | Doctor Todd Smith<br>W. W. Hansen Experimental Physics Laboratory<br>Stanford University<br>Stanford, California 94305-4085   | 1 |
| 10. | LCDR Roger M. Mabe<br>Route 3 Box 192<br>King, North Carolina 27021   | 2 |